Observations of Moderate to Deep Seasonal Snow in Agricultural Fields with a Radar Scatterometer at Ku- and X-band Frequencies

by

Aaron Thompson

A thesis
presented to the University of Waterloo
in fulfillment of the
thesis requirement for the degree of
Master of Science
in
Geography

Waterloo, Ontario, Canada, 2015

Author's Declaration

I hereby declare that I am the sole author of this thesis. This is a true copy of the thesis, including any required final revisions, as accepted by my examiners.

I understand that my thesis may be made electronically available to the public.

Abstract

The water contained within a snowpack, or the snow water equivalent (SWE), is very important to the hydrological cycle and to populations who depend on it for drinking, agriculture and industry. Measuring SWE over large areas is therefore important, but difficult given the scale of such an endeavor. Radar remote sensing of snow offers the promise of measuring SWE remotely but before we can do so, we must better understand how microwaves and snow interact.

This thesis investigates the interaction of Ku- and X-band radar with moderate to deep seasonal snow in agricultural fields over two winters in Ontario. The University of Waterloo Scatterometer (UW-Scat) was used to make measurements of both snow-covered and snow-free fields in Maryhill and Englehart Ontario spanning a range of SWE up to 186 mm. In the 2013-14 season, 4 observations were made in Maryhill. In the 2014-15 season 3 sites were revisited over 6 dates in Maryhill and 3 sites were visited in Englehart. Accompanying the radar observations, *in situ* observations of snowpack properties including depth, density, stratigraphy, and grain size estimation were made at each site. Sensitivity to SWE was observed at Ku-band but not at X-band. An upper limit of sensitivity was observed around 140 mm after which point, Ku-band backscatter no longer responded to increasing SWE. However an investigation of seasonal depth hoar evolution suggested that the presence of depth hoar layers within the snowpack was the primary influence on backscatter response. Polarimetric data indicated the signal from early season, low-accumulation snowpacks was driven by vegetation where present and this influence decreased with further accumulation of snow.

The major contribution of this study is the identification of depth hoar layers as a driver of backscatter response. This outcome points the way to further research on the influence of depth hoar, especially the mechanisms by which it exerts influence on the signal. Another contribution of this study is the identification of early-season influence of agricultural vegetation on backscatter through the use of polarimetric information.

Acknowledgements

First and foremost, I would like to thank my supervisor, Dr. Richard Kelly, for his guidance, encouragement and support throughout this journey and for having the patience to allow me great independence in both my studies and in my field work; I often learn as much through my mistakes as I do through my successes. I'm looking forward to the PhD.

Active microwave remote sensing is complicated. UW-Scat is complicated. The help of great mentors along the way has been essential to my success. For their role in this capacity I would like to acknowledge and thank Josh King, Andrew Kasurak, and Grant Gunn. From you I have learned many of the things you can't learn from books, and without your help I may still be sitting in the lab watching the scats spin in circles and wondering.

Without the support of friends and a great field crew this project could not have happened. For their hard work, early mornings, and frozen extremities, I would like to thank Vicky Vanthof, Qinghuan Li, Jessie Tang, Soroosh Bordbar, Mike Brady, Nastaran Saberi, Jeff Chan, and John Coughlin. I would also like to thank the land owners, John Nederland and John Vanthof, who allowed access to their land for this study.

I would like to express gratitude to my girlfriend Vigy, who by this point has learned everything she never wanted to know about radar and snow. She has faithfully watched me practice presentations, listened to me explain how the scats work, and tried her best to understand my results. Above all else, she has kept me sane and well fed.

Finally, I would like to thank my family whose support and encouragement, while I pursue my academic goals, has always meant the world to me.

Table of Contents

List of Tables

List of Figures

Chapter 1 Introduction

1.1 Context and motivation

Snow is an important source of freshwater that supports ecosystems, agriculture, industry, and the municipal water supply (Pomeroy et al., 2009). Characterizing and quantifying the snow state, especially the snow water equivalence (SWE), is important for water resource management and energy balance modelling because it is an indication of the volume of water available for runoff (Rott et al., 2010; Shi & Dozier, 2000). According to Barnett et al. (2005) snow plays a large role in the cryospheric energy balance by moderating atmospheric and surface heat exchange and the study of snow can help us to understand multi-scale climate systems and regional hydrology. Climate change is having an impact on snow extent and duration globally but some regions, such as the Northern high latitudes, are experiencing these changes at rates nearly twice that of the rest of the world and this realization is emphasizing the need for a practical means of monitoring these changes with a high temporal and spatial resolution (Derksen & Brown, 2012). This has prompted organizations such as the World Meteorological Organization to articulate the need for high-resolution SWE observations (IGOS, 2007). Traditionally, these observations often relied on a network of *in situ* snow observations by way of snow pits, but the frequently rough, irregular, and inaccessible terrain makes it difficult and impractical to gather enough measurements (Shi & Dozier, 2000). Active microwave, or radar, remote sensing has gained attention as a way of measuring snow properties at high spatial and temporal scales because of its observed response to snow depth, liquid content, stratigraphy, surface features, grain size, and grain shape (Colbeck, 1982b; Du et al., 2010, & King et al., 2013). Another benefit to radar remote sensing is its non-destructive nature. Koh et al. (1996) identified situations where the destructive nature of snow pits masked transitions in a snow cover

that were only detected using radar. In general terms the usefulness of a radar system on snow observations stems from its frequency-dependent response to grain characteristics, liquid water content, and stratigraphy (Dierking et al., 2012; Strozzi & Mätzler, 1998).

Previous studies have investigated the radar response of snow using both ground-based and airborne platforms at various frequencies to extract information about snowpack properties and quantities (Kendra et al., 1998; King et al., 2013; King et al., 2015; Lemmetyinen et al., 2011; Marshall et al., 2004; Marshall et al., 2005; Strozzi & Mätzler, 1998; Yueh et al., 2009, among others), many with a particular interest in SWE. These studies indicate that such observations can yield important information on snowpack characteristics and volume, with potential for retrieval over large areas and over those areas otherwise unreachable. Studies such as the CoReH_2O Snow and Ice Experiment (Can SCI) in 2009-10 and the Canadian Snow and Ice Experiment (CASIX) in 2010-11, employed ground based radar at Ku- and X-band frequencies to observe snow properties in the Canadian subarctic (King et al., 2013). In 2002-03 and 2006-08, the NASA Cold Lands Processes mission (CLPX) and CLPX-II used ground-based Ku-, X-, and C-band and airborne Ku-band measurements to observe snow in the Colorado Rocky Mountains (Yueh et al., 2009). These studies reported a relationship between Ku-band backscatter and SWE in which backscatter increased with SWE. Results of CASIX showed that co-polarized vertical backscatter increased by 0.82 dB per 1 cm increase in SWE while during CLPX-II a rate between 0.15 – 0.5 dB per 1 cm increase in SWE was observed (King et al., 2015; Yueh et al., 2009). Furthermore, the authors of these studies made similar inferences that the presence of depth hoar in the snowpack might contribute to an elevated backscatter response although their conclusions differed in terms of the polarization of the resulting preferentially scattered wave.

Another characteristic these studies had in common is that they observed snow in either high-latitude or high-altitude environments. Collectively these sites have cold snowpacks and experience long, cold, winter seasons with minimal mid-season warming episodes and rain events (Sturm et al., 1995). However, there have been no studies found that make active microwave observations of continental, mid-latitude snowpacks in agricultural fields such as those found in much of Ontario. According to the snow cover classification by Sturm et al. (2010) shown in **Figure 1.1**, the snow cover class in southwestern Ontario is maritime, characterized by a warm, deep, snow cover with commonly occurring melt features, and high wind exposure. Therefore this environment is very different from those observed thus far in active microwave studies and it follows that the interaction between snow and microwaves in a maritime snowpack could be driven by very different processes such as the development of ice features within the pack and snowmelt conditions. Vegetation beneath the snowpack will influence the radar response as Yueh et al. (2009) observed, however the influence of agricultural crops, often characterized by regular spatial distribution and homogenous size and shape could lead to unique subnivean scattering signatures. Furthermore, considering the areal extent of the maritime class in **Figure 1.1**, this class covers a heavily populated area of North America, spanning much of the mid- to northeastern portion of the continent, with much of that being agricultural land. Therefore understanding snow property retrieval with active microwave remote sensing is of great interest. With this in mind this thesis focuses on radar observations of moderate to deep seasonal snow in agricultural fields with a scatterometer at Ku- and X-band frequencies.

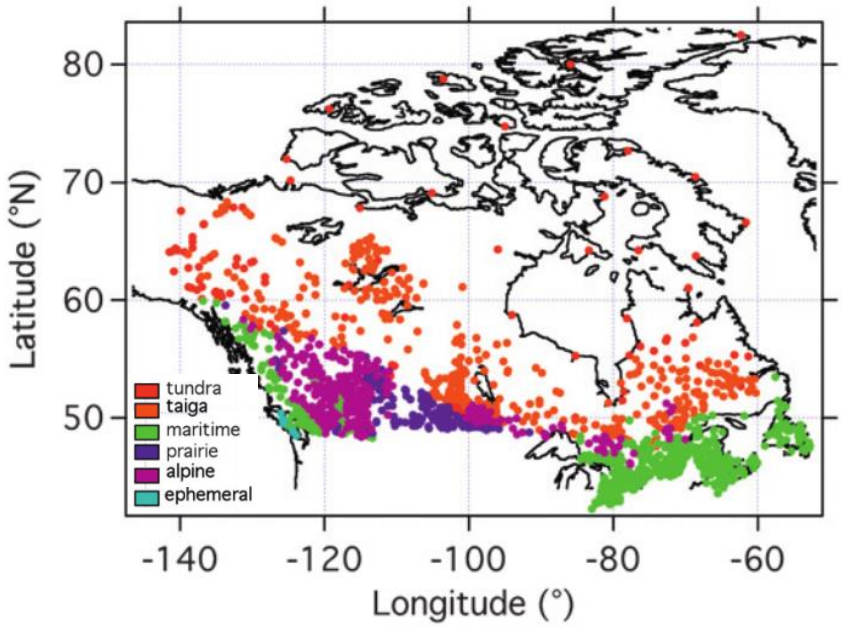

Figure 1.1 Snow cover classification system by Sturm et al. (2010). Snow cover in southwestern Ontario is classified as maritime.

1.2 Aims and objectives

The overall aim of this thesis is to explain the backscatter response of Ku- and X-band scatterometer signals from deep seasonal snow in agricultural fields in Ontario. To achieve this, three specific objectives were defined as:

1) To quantify and characterize the active microwave backscatter response to a range of seasonal snow at 9.6 and 17.2 GHz;
2) To explain the polarimetric response in this environment;
3) To develop a field data set to test microwave scattering models for snow accumulation in an agricultural field.

1.3 Thesis structure

This thesis has been written following the manuscript structure in which a standalone paper is included as a separate chapter. Chapter 2 provides background information on active microwave remote sensing, snow and the interaction between the two. Chapter 3 is comprised of a paper entitled *Ku- and X-band radar observations of deep seasonal snow in agricultural fields in Ontario*. It is the intention of the author to submit this paper to the IEEE Geoscience and Remote Sensing Letters. The final chapter summarizes and concludes the thesis and provides direction for future work.

Chapter 2 Background

2.1 Radar equation

The most basic function of a radar system is to measure a target distance through the time delay of an echo. In order to determine whether or not a radar echo can be detected the radar equation is used to describe the power returned to the sensor for a known incident power transmission (Woodhouse, 2006). The development of this equation traces the radar signal from its propagation at the transmitter, to the target, and back to the receiver. This represents a monostatic radar system, in which the transmitter and receiver are co-located.

Energy is initially transmitted in all directions from the antenna. To determine power density at the target power transmitted (P_t) is reduced by a spreading loss which describes the loss of power as the energy propagates in a spherical pattern, of radius R, from the antenna surface (Ulaby et al., 1982). The power is focused in a specific direction by applying a gain factor (G). The power intercepted and scattered by the target becomes:

$$power\ density\ at\ \ target = \frac{P_t G}{4\pi R^2} \tag{2.1}$$

An amount of incident energy proportional to the target surface area (A_s) is intercepted by the target and a portion is absorbed (α) while the rest (1-α) is reflected. G is applied towards the receiver and the following describes the radar cross section of the target (σ):

$$\sigma = A_s(1-\alpha)G \tag{2.2}$$

The value of σ is the expected surface area of the target under the assumption that the area σ intercepted the incident wave and scattered it isotropically; however it is not necessarily related to the actual size of the target. The target may appear smaller than it is when value of σ approaches 0 in the case that energy is scattered away from the antenna or the target is absorbent,

while it may appear much larger if the target scatters more energy back to the antenna than is expected from an isotropic scatter (Woodhouse, 2006). The scattered power returns to the antenna whose aperture (A_r) is described in terms of the transmitted wavelength (λ) and G:

$$A_r = \frac{\lambda^2 G}{4\pi} \tag{2.3}$$

The power received at the antenna (P_r) is then found by combining 2.1 through 2.3 and reducing it once more by a spreading loss from the target to provide the monostatic radar equation:

$$P_r = \frac{P_t G^2 \lambda^2 \sigma}{(4\pi)^3 R^4} \tag{2.4}$$

Rearranging 2.3 allows us to solve for σ which is typically normalized by the illuminated area (A) to provide the normalized radar cross-section (σ^o):

$$\sigma^o = \frac{\sigma}{A} = P_r \frac{(4\pi)^3 R^4}{A P_t G^2 \lambda^2 \sigma} \tag{2.5}$$

Normalization is applied since the target in Earth observations is usually distributed over an area and increasing the measured area would increase σ by the same factor since σ corresponds to the size of the instrument footprint (Woodhouse, 2006); such is the case for snow in an agricultural field. Normalizing σ by the illuminated area allows us to compare measurements from different instruments (Woodhouse, 2006). Since the value of σ^o can vary by several orders of magnitude, it is converted from a linear scale to a logarithmic scale, expressed in decibels (dB).

2.2 System parameters

Revisiting (2.4) we note that of all the variables on the right-hand side, only σ is controlled by the target properties while the remaining variables are known system parameters (Woodhouse, 2006). It follows that by keeping those system parameters constant and solving for P_r we can isolate the influence of the target properties. Therefore knowing and understanding system parameters such as frequency, polarization and incident geometry is critically important.

2.2.1 Frequency

The microwave portion of the electromagnetic spectrum ranges in frequency from about 0.3 to 300 GHz although radar systems typically use frequencies from 1 to 90 GHz (Ulaby et al., 1981, Woodhouse, 2006). Within this range, Earth observations usually occur at frequencies below 20 GHz to avoid interaction with the atmosphere (Ulaby & Long, 2014). Frequency (f) is related to λ by the speed of light (v) through the following relationship:

$$\lambda = \frac{v}{f} \tag{2.6}$$

Changing λ influences the interaction of the incident wave with the target medium especially as λ approaches physical dimensions of a scale similar to the target as a discussion on scattering theory and surface roughness in subsequent sections will show. The penetration depth (δ_p) of a wave in a medium is dependent on λ and is determined for snow as:

$$\delta_p = \frac{\lambda\sqrt{\varepsilon\prime}}{2\pi\varepsilon''} \tag{2.7}$$

Where ε' and ε'' are the real and imaginary portions of the relative permittivity. **Figure 2.1** demonstrates the frequency dependence of the relationship between δ_p and liquid water content.

Lower frequencies are associated with greater δ_p however in reality δ_p may be less due to scattering losses (Ulaby et al., 1984).

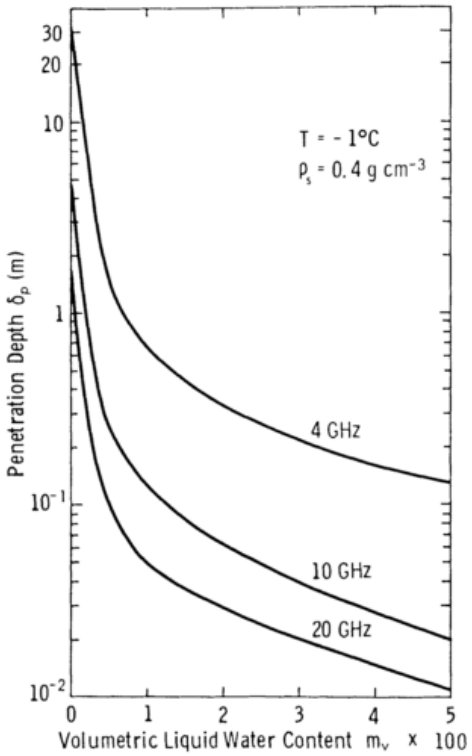

Figure 2.1 Relationship between penetration depth in snow and liquid water content for different frequencies (from Ulaby et al., 1984).

2.2.2 Polarization

Electromagnetic waves consist of time-varying electric and magnetic fields but by convention we only consider the electric field when characterizing a wave (Woodhouse, 2006). Such waves are transverse which means they oscillate in a plane perpendicular to their direction of travel (Elachi et al., 1990; Ulaby & Long, 2014). The nature of the oscillation of these waves, or their polarization, is described in terms of an orthogonal basis in the plane of oscillation which allows us to characterize all possible polarization states (Woodhouse, 2006). The axes of this basis are referred to as vertical (V) and horizontal (H) in reference to the surface of the Earth. The polarization ellipse shown in **Figure 2.2** is used to visualize the polarization state of a wave

in terms of its ellipticity (χ), orientation angle (ψ), and the X and Y components of the electric field (E_x and E_y).

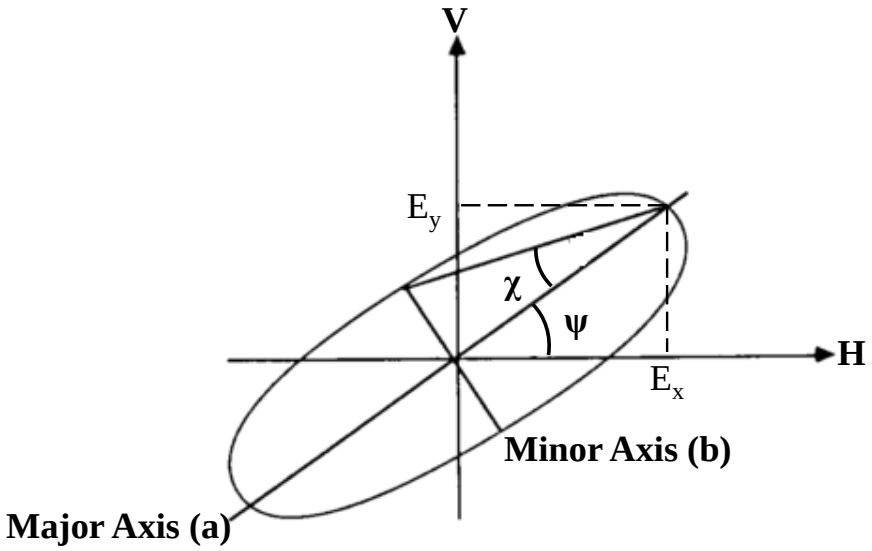

Figure 2.2 Polarization ellipse adapted from Evans et al. (1988).

The shape of the ellipse is governed by χ which is determined by:

$$\chi = tan^{-1}\left(\frac{b}{a}\right) \tag{2.8}$$

where a and b are the major and minor axes of the polarization ellipse. According to Ulaby & Long (2014), the polarization is linear when the phase difference between E_x and E_y is 0 (in phase) or π (out of phase) radians, corresponding with χ of 0°. The polarization is circular when phase difference between E_x and E_y is +/- π/2 which occurs when components of the electric field are equal (Ulaby & Long, 2014). This corresponds to a χ of +/- 45°. The orientation of the ellipse is governed by ψ and ranges from 0° to 180°; its calculation follows:

$$\psi = tan^{-1}\left(\frac{|E_x|}{|E_y|}\right) \tag{2.9}$$

The case of horizontal polarization occurs when ψ is 0° or 180° while vertical polarization occurs when ψ is 90°.

Comparing the polarization state of the incident and scattered wave can provide useful insight into the nature of the target through its interaction with the wave. A co-polarized response occurs when the polarization state of the scattered wave is the same as the incident wave and is indicative of a first-order scattering mechanism. A cross-polarized response occurs when the polarization state of the scattered wave has been changed through interaction with the target. This is known as depolarization and through such interaction the wave is depolarized. This can occur with higher-order scattering mechanisms such as multiple-bounce or volume scattering. Preferential scattering may occur when target features are aligned with the incident polarization such as the increase in vertical scattering which occurs for vertically oriented crops (Woodhouse, 2006). As an example, King (2015) suggested that vertical orientation of depth-hoar crystals in a snowpack contributed to an elevated vertical response.

2.2.3 Incidence geometry

There are two primary ways in which the incidence geometry can influence wave propagation one of which occurs at the air-target interface and the other within the volume of the target medium. Assuming a smooth surface, a portion of the incident wave will be reflected at the air-target interface and a portion will be transmitted into the target medium for a given incidence angle (θ_i). Fresnel's reflection coefficients (R_{VV} and R_{HH}) are used in determining this proportion for both vertical and horizontal polarizations. Finding the square of R_{VV} and R_{HH} provides the reflectivity, or the proportion of reflected energy:

$$(R_{VV})^2 = \left(\frac{\varepsilon \cos\theta_i - \sqrt{\varepsilon - \sin^2\theta_i}}{\varepsilon \cos\theta_i + \sqrt{\varepsilon - \sin^2\theta_i}}\right)^2 \quad (2.10)$$

$$(R_{HH})^2 = \left(\frac{\cos\theta_i - \sqrt{\varepsilon - \sin^2\theta_i}}{\cos\theta_i + \sqrt{\varepsilon - \sin^2\theta_i}}\right)^2 \quad (2.11)$$

Reflectivity ranges from 0, or total transmission, to1, which indicates total reflection. Vertically and horizontally polarized waves behave differently in terms of reflectivity, except for at nadir when they are equal (Woodhouse, 2006). Horizontal reflectivity increases monotonically with θ_i toward total reflection at the grazing angle, where θ_i is 90°. The reflectivity for vertical polarization decreases to a minimum, before reaching total reflection at the grazing angle. This minimum is known as the Brewster angle at which point total transmission of the vertically polarized wave occurs (Ulaby et al., 1981). **Figure 2.3**, calculated from 2.10 and 2.11 where ε_{snow} is approximated to be 2, illustrates this concept.

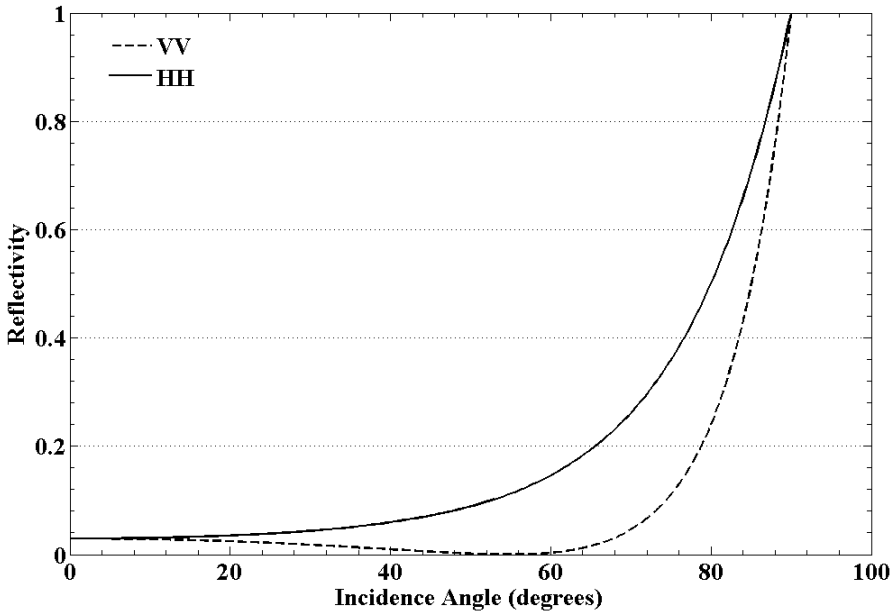

Figure 2.3 Reflectivity for VV and HH polarizations calculated from Fresnel coefficients where ε of snow was approximated to be 2.

The shortest path through a medium results when θ_i =0°, at Nadir. With an increase in θ_i, the path length of the incident wave through the target media is extended. As the path length grows, so does the potential for scattering within the volume as the wave will have more chance to interact with scatters in the media, such as snow grains (King et al, 2015).

2.3 Target parameters

Once all of the system parameters have been accounted for, changes in P_r may then only occur from temporal or spatial changes in target properties. These properties include the dielectric properties of the snowpack, roughness, and the state of development of the snowpack which includes variables such as grain size, liquid water content, density, stratigraphy and the underlying soil roughness and dielectric state.

2.3.1 Dielectric properties

Most materials encountered in remote sensing are considered dielectric, which means they are non-conducting (Woodhouse, 2006). A snowpack can be thought of as a dielectric mixture composed of air, ice particles, and liquid water and so its dielectric behavior is relative to the proportion of its constituents (Hallikainen et al., 1986). The dielectric behavior of a medium is described by its relative permittivity (ε_r). This is a complex number wherein the real portion (ε') describes the ability of the medium to store energy, while the imaginary portion or loss factor (ε'') describes the dissipation of energy, and $i = \sqrt{-1}$:

$$\varepsilon_r = \varepsilon' - i\varepsilon'' \tag{2.12}$$

For dry snow, the real component of relative permittivity (ε_{ds}') is governed primarily by density (ρ_{ds}) and can be estimated using a linear model (Tiuri at al., 1984):

$$\varepsilon'_{ds} = 1 + 2\rho_{ds} \tag{2.13}$$

Using this model we find that ε_{ds}' ranges from about 1.2 – 2 for snow densities between 100-500 kg m^{-3}. Tiuri et al. (1984) provide the imaginary component of the relative permittivity of dry snow (ε_{ds}'') as a ratio with ε_{ice}'':

$$\frac{\varepsilon_{ds}''}{\varepsilon_{ice}''} = 0.52\rho_{ice} + 0.62\rho_{ice} \quad (2.14)$$

It is common in remote sensing applications to refer only to ε' in discussion of relative permittivity. Commonly referenced values of ε' include that for air, ice, soil and water (1, 3.17, 2.2-4 and 80) (Du et al., 2010; Marshall & Koh, 2008; Woodhouse, 2006; Yueh et al., 2009). When liquid water is present in the snowpack, such as during melting or rain events, the relative permittivity increases. Through an increase in ε'' with liquid water, this may lead to increased attenuation and less scattering from the snow volume (Ulaby & Stiles, 1981). Discontinuities in ε' across boundaries can contribute to a strong radar response through enhanced surface scattering (Marshall et al., 2007). Revisiting Fresnel's reflection coefficients discussed in Section 2.3.3 (equations 2.10 and 2.11), note that an increase in ε', which occurs as the liquid water content of the snowpack increases, causes an increase in reflectivity at the snowpack surface. For this reason, Kendra et al. (1988) observed an increase in backscatter from the surface of a wet snowpack.

The velocity (v) of a wave travelling in a vacuum (c) is roughly $3x10^8$ m s^{-1} but when travelling through a dielectric medium it is reduced (Woodhouse, 2006). Thus relative permittivity plays a role in the speed of wave propagation:

$$v = \frac{c}{\sqrt{\varepsilon r}} \quad (2.15)$$

Relative permittivity is related to the index of refraction (n) through the following relationship:

$$n = \sqrt{\varepsilon}' \tag{2.16}$$

When a wave is transmitted across a surface boundary from one medium into another, the speed of propagation will change if the two mediums have a different index of refraction and this will result in a redirection of the incident wave towards or away from the normal (Woodhouse, 2006). This is referred to as refraction and is governed by Snell's law:

$$\frac{sin\theta_i}{sin\theta_r} = \frac{v_1}{v_2} = \frac{n_2}{n_1} \tag{2.17}$$

Here θ_r is the angle of refraction, n_1 is the index of refraction for the first medium, n_2 is that of the second and v_1 *and* v_2 are the initial-wave and refracted-wave velocities. This relationship must be accounted for at each surface through which a wave passes, given a difference in n. In a medium with multiple stacked layers such as most snowpacks, refraction may occur multiple times in a wave's path. Combining (2.13), (2.15), and (2.16) in Snell's law it becomes apparent that an increase in snowpack density will increase ε', thereby increasing n and reducing v. This reduction in speed will then reduce the angle of refraction as the wave enters the medium provided that it is entering from a medium with a lower index of refraction, such as air.

2.3.2 Roughness

A smooth surface is defined as one in which surface features are of a size much smaller than the incident wavelength (Woodhouse, 2006). From such a surface, a portion of the wave, as governed by the Fresnel coefficients, is coherently reflected in the specular direction, meaning no change in phase has occurred with the reflection. As the surface becomes rougher, scattering will become increasingly diffuse. The Fraunhoffer criterion defines roughness for microwave

applications by comparing the root mean square (rms) height deviation of surface features (h_{smooth}) to the wavelength for a given θ_i:

$$h_{smooth} = \frac{\lambda}{32cos\theta_i} \tag{2.18}$$

Any surface features smaller than the criteria are considered smooth, while any features larger are considered rough. The relationship described in (2.18) demonstrates that this threshold is larger for larger λ but decreases as θ_i increases. In the case of a dry snowpack, roughness at the air-snow interface is inconsequential because the dielectric mismatch is negligible and so scattering at the snow surface usually neglected (Ulaby et al., 1986). However the roughness of the air-snow interface may become important in a wet snowpack where there is sufficient dielectric discontinuity introduced by water in the pack (Kendra et al., 1998, Ulaby et al., 1984). In a dry snowpack the roughness of the soil beneath can contribute to the scattering of an incident wave because of the dielectric mismatch between the snow and the soil. Furthermore the impact of soil beneath a snowpack can vary in time due to changes in its freeze-thaw state (Shi, 2004)

2.3.3 Snowpack development

The snowpack characteristics that are most influential in terms of radar remote sensing are snow grain size and shape, liquid water content of the snowpack, and snowpack stratigraphy. While snow grain size and shape are examples of grain-scale influences, liquid water content is considered at small and large scales, and stratigraphy can influence snowpack characteristics at scales up to hundreds of metres (Sturm & Benson, 2004).

Grain characteristics

Colbeck (1982a) divided snow into four categories: dry snow in equilibrium form, dry snow in kinetic growth form, wet snow in the pendular regime, and wet snow in the funicular regime. Dry snow in the equilibrium state is rounded and grows slowly in the absence of temperature and pressure gradients where vapour diffusion is the rate-limiting process (Colbeck, 1980). Larger crystals grow at the expense of smaller ones which sublimate, driven by diffusion of water vapour among grains with different radii of curvature whereby those grains with smaller radius of curvature become vapour sources and those with a larger radius of curvature become vapour sinks (Colbeck, 1980). This form of snow most commonly controls grain shape in the absence of large temperature gradients (Colbeck, 1982a). While radius of curvature initially controls metamorphism of fresh snow, once the smaller dendrites disappear, metamorphism becomes controlled by temperature and vapour (Colbeck, 1980). When dry snow is exposed to vapour fluxes and large temperature gradients, especially those greater than 10 °C/m, kinetic growth occurs, the grains crystallize, and becomes faceted (Colbeck, 1982a; Sturm & Benson, 1997); the most highly developed configuration of such form is a hollow sheath or cup known as depth hoar (Colbeck, 1982a). Metamorphism into depth hoar is also accompanied by a reduction in the number of grains (Sturm & Benson, 1997). Similar to depth hoar, large, faceted crystals known as surface hoar can develop at the snow surface, typically in shaded areas, and in the presence of a downward vapour gradient and radiative snow surface cooling (Helbig & van Herwijnen, 2012). These faceted crystals are unstable without a large temperature gradient and so they revert back to the rounded equilibrium form once the gradient has been removed (Colbeck, 1982a).

Grain size and shape have a substantial impact on the radar return and backscattering since ice particles within snow are considered to be densely distributed scatterers whose inter-granular spacing is much less than the incident wavelength at microwave frequencies (Shi & Dozier, 2000). Scattering from snow is close to the limit between Rayleigh and Mie scattering and therefore the appropriate scattering theory is frequency dependent (Shi & Dozier, 2000); this will be discussed further in Section 2.4. Small, fine snow grains, such as those fractured by wind and packed into dense wind slab can reduce backscatter, leading to a weaker radar return; however the electromagnetic energy at relatively lower frequencies will penetrate through such a layer (Dierking et al., 2012). As the size of spherical grains increase within the snowpack, so does volume scattering which drives depolarization, and therefore an increase in cross-polarized backscatter may be realized (Yueh et al., 2009). Larger, aggregate particles which form when individual grains freeze together, such as during melt-refreeze events, similarly lead to an increase in backscatter (Kendra et al., 1998). Grain size also has a frequency-dependent impact on the ability of electromagnetic energy to penetrate a snow pack. Koh et al. (1996) observed a reduction in penetration in the presence of large-grained depth hoar at 40 GHz, and speculated that a reduction in penetration at X-band could occur if the grains continued to grow. Faceted crystals impact the radar return at microwave frequencies due primarily to their larger surface area and alignment which is caused by the vertical vapour fluxes associated with their growth (Colbeck, 1982a). Koh et al. (1996) observed a stronger HH response in the presence of horizontally aligned crystals while King et al. (2013) found a stronger VV response in the presence of vertically aligned crystals.

Liquid water content

When liquid water is introduced into a snowpack, the snow grains grow rapidly, becoming rounded and larger grains grow at the expense of the smaller ones (Marsh, 1987). **Figure 2.4** illustrates how grain growth in saturated snow increases with time; note the increase in variation of grain size in time.

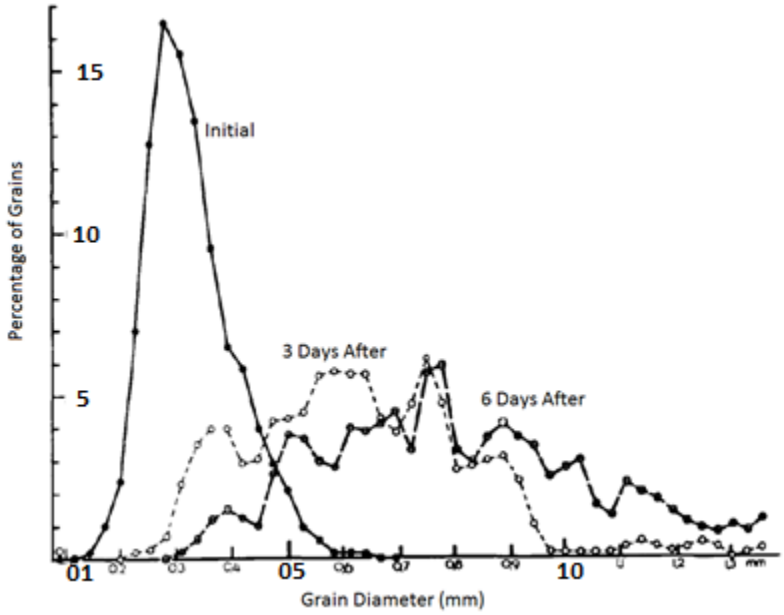

Figure 2.4 Change in size and distribution of grains in water-saturated snow from time of initial wetting (Wakahama, 1965).

A difference in radii creates a heat flux from larger grains to smaller grains and since this heat flux moves predominantly through the liquid-solid interface, the growth rate increases with water saturation (Marsh, 2005). Colbeck (1980) emphasized the fact that for grain growth in water-saturated snow, the rate-limiting process is heat flux instead of vapour flux as it is for dry snow. Wakahama (1965) determined that grains with a smaller radius have a much lower melting point than larger grains in saturated snow. Grain growth and rounding in saturated snow, which can occur in only hours and a few days respectively, is typically much faster than in dry snow where the same amount of growth would theoretically take years (Colbeck, 1980). In the pendular

regime, tightly packed grain clusters dominate, whereas well-rounded, singular, cohesionless particles appear in the funicular regime (Colbeck, 1982a). At water contents greater than 30% the ice matrix dissolves into separated ice grains (Marsh, 2005). As with dry snow, growth in unsaturated wet snow is driven by vapour diffusion whereby vapour pressure is higher over small grains and therefore growth is much slower than in saturated wet snow (Colbeck, 1980). If such snow experiences melt-refreeze conditions, the grains can freeze together to form larger polycrystalline grains (Marsh 1987).

Liquid water in the snowpack causes ε' to rise substantially and thus increases signal attenuation and any scattering will result from interaction with the air-snow interface (Koh et al., 1996; Shi & Dozier, 2000; Marshall & Koh, 2008). **Figure 2.5** illustrates this. Most of the variability in radar backscatter within a snowpack is attributable to the presence and absence of liquid water therefore it is one of the most influential characteristics (Strozzi & Mätzler, 1998). The large dielectric contrast between water, ice and air is responsible for this and allows radar to be used effectively to monitor melt-freeze processes in a snowpack (Marshall & Koh, 2008). This effect is so strong that radar can be used to detect even small regions of wet snow which allows the detection of features such as flow fingers within a snowpack (Albert et al., 1999).

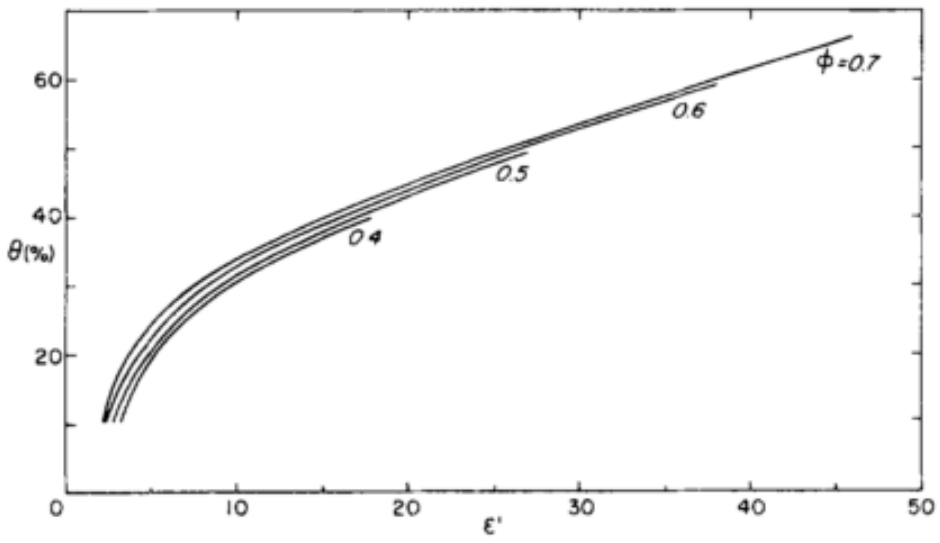

Figure 2.5 Permittivity versus liquid water content (θ) (from Colbeck, 1982b). Permittivity rises rapidly with liquid water content for different values of snowpack porosity (φ).

While liquid water in a snowpack can reduce backscatter, there are situations where an increase in backscatter may be observed instead. Kendra et al. (1998) observed such a result from a wet snowpack that contained an ice lens near the surface during a period of warm air temperatures, resulting in an increase in backscatter due to surface scattering from the air-snow interface which outweighed a reduction in volume scattering due to signal attenuation caused by the water content. In melt-refreeze conditions where grain growth has occurred before refreezing, backscatter can be enhanced by the presence of larger and especially polycrystalline grains. Diurnal melt-freeze cycles have also been characterized with radar. In some cases, colder temperatures at night freeze any liquid water resulting in higher backscatter but during the day, warm temperatures lead to melting which increases the water content concomitantly decreasing backscatter, except where enhanced surface scattering occurs (Kendra et al., 1998; Strozzi & Mätzler, 1998).

Density

Density of snow is defined by Fierz et al. (2009) as the mass per unit volume of snow. Snow density, which varies spatially (both horizontally and vertically) and temporally, can influence the electrical, thermal, and mechanical properties of snow (Bormann et al., 2013). Field estimates of snow density are completed by extracting a known volume of snow using a cutter and weighing it: Density is then calculated by dividing the sample mass by the sample volume. Tiuri et al. (1984) found that the permittivity of dry snow increased linearly with snow density, while that of wet snow increased with liquid water content. **Figure 2.6** illustrates the relationship and provides two models used to approximate ε' of dry snow. The authors suggest the polynomial model may over-fit in some cases and that the linear model is generally preferred.

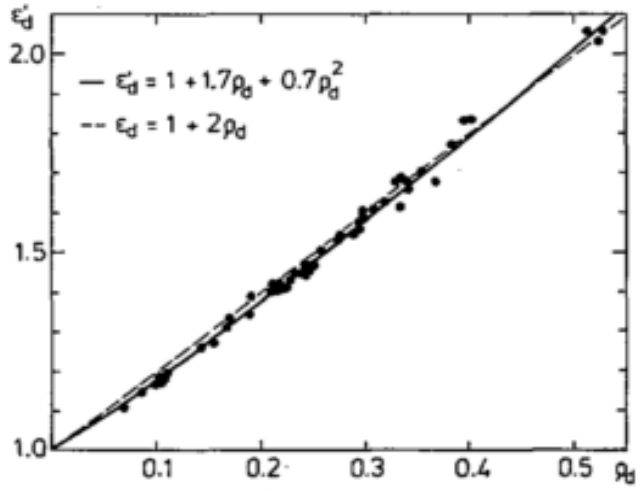

Figure 2.6 A linear and second-order polynomial model used to estimate the permittivity of dry snow using density. Density of dry snow (g cm^{-3}) is shown on the x axis and the real permittivity of dry snow is shown on the y axis (from Tiuri et al., 1984).

The density of snow ranges from around 100 kg/m^3 for freshly fallen, dry snow, to 500 kg/m^3 for wet snow (Fierz et al., 2009). Factors that can impact density can be divided into mechanical and thermal processes.

The mechanical processes influencing density include compaction and wind redistribution. Compaction involves mechanically compressing the snow which leads to a higher density. On a small scale, compaction can occur from trampling the snow, however on the large scale of concern to remote sensing compaction is associated with snow accumulation through the addition of newly fallen snow (Sturm et al., 2010). As snow accumulates, more weight is placed on snow at the bottom of the snowpack which leads to its densification (Bormann et al., 2013; Langlois et al., 2007). Wind can play a crucial role in densification through redistribution and alteration of snow deposition patterns (Lopez-Moreno et al., 2013). As wind blows the snow, the structure of the crystal becomes rounded, allowing the flakes to become more tightly packed (Bormann et al., 2013), with potential to increase the snowpack density beyond 400 kg/m^3 in cases of so-called wind slab (Marshall, 2012). Wind can move snow from flat surfaces, windward slopes, and sparsely vegetated areas and deposit it on leeward slopes, in depressions, and in more heavily vegetated areas (DeBeer et al., 2009; MacDonald et al., 2010). The snow collects or drifts where there are turbulent eddies or convergence of wind flux (Marshall, 2012). This can lead to a localized densification due to the compaction of underlying layers, and through creation of wind slab in cases of persistent wind.

The thermal factors that influence density include temperature changes and solar radiation. Temperature changes can increase and decrease snowpack density. In periods of warm weather, the snow grains begin to melt, simultaneously becoming rounder in shape allowing for closer spacing within the snowpack, and increasing the liquid water content of the snow (Lopez-Moreno et al., 2013). This has a combined effect that increases the density of the snowpack, and explains why a density increase in the snowpack can be seen in the transition from winter to spring. Temperature can also contribute to a decrease in density within a dry

snowpack where a temperature gradient exists between the base of the snowpack and the air-snow interface. Such conditions promote water-vapour transport within the snowpack and lead to the development of depth hoar in the snowpack where water vapour sublimate from the top of an ice grain and condense on the bottom of an another above (Sturm & Benson, 1997). The size and shape of these grains prevent them from packing tightly, decreasing the snowpack density (Bormann et al., 2013).

Solar radiation is a major driver of many snow processes (Schweizer & Kronholm, 2007). Among other things, exposure to shortwave solar radiation can eliminate surface hoar, although an accurate threshold at which enough shortwave radiation is present to do so is unknown (Helbig & van Herwijnen, 2012). Intuitively this process can be linked with increasing the snow density through the replacement of the large, faceted, surface hoar crystals with smaller, more tightly packed varieties however Bormann et al. (2013) indicated that the link between snow density and solar radiation has not yet been well established.

Stratigraphy

Sturm and Benson (2004) described a snow layer as a tabular body that has unique characteristics which distinguish it along well-defined boundaries from newer snow above, and older snow beneath. Layers are formed and influenced by snowfall, wind, compaction, snow melt and snow metamorphism; unique combinations of these processes contribute to identifiable layer characteristics with sufficient speed such that snow deposited for even just one day can experience remarkable change (Marsh, 2005). Because the nature of a layer is dependent on its microstructure, Sturm and Benson (2004) assert that layering and grain characteristics are inextricably linked. Layers are often indicative of climatic conditions and meteorological episodes and thus tell a story about the magnitude and timing of events that occurred during the

lifespan of the snowpack such as temperatures fluctuations and gradients, melt-freeze conditions and ice rain. Forster et al. (1991) used pairings of depth hoar and wind crust layers to identify the autumn and winter for a given year in Antarctica. Thermal conditions within a snowpack can be identified by stratigraphy as well. Marsh and Woo (1984) explained that a basal ice layer will form in liquid saturated snow when a negative heat flux exists at the ground-snow interface such that heat moves into the soil from the snow, causing the saturated snow to freeze.

According to Sturm and Benson (2004), due to a lack of comprehensive data there are two different views on layering: In one, layers are assumed to be laterally homogenous and a good foundation for extrapolating snowpack characteristics. In the other view, layers are assumed to be so heterogeneous that cross-correlation is difficult or impossible especially at larger scales. Marsh (1987) found that strata in the Arctic were undulating but generally parallel and were continuous up to about 3 m. Sturm and Benson (2004) examined layer heterogeneity over distances up to 100 km and determined that perennial snow layers were more uniform and laterally continuous than seasonal layers, but that the heterogeneity of the two classes converged at scales of about 100 m at which point the layer heterogeneity was maximized; this distance corresponds with the scale of wind drift features. As such they indicated that local forcing by weather, especially wind and temperature was the primary driver of heterogeneity at this scale but that synoptic scale variations also contributed. The microtopography underlying the snowpack had a stronger effect on seasonal snow than on perennial snow whose layers tended to vary less since the impact of wind-snow interaction triggered by microtopography was minimized (Sturm and Benson, 2004).

Discontinuities in permittivity that are introduced with varying layer characteristics such as density, grain size, presence of ice layers or pillars, and liquid water content can influence

backscatter (Marshall et al., 2007). Ice layers present within the snowpack can reduce the penetration of frequencies with relatively shorter wavelengths as Marshall & Koh (2008) found, which necessitated the use of longer wavelengths. Marshall et al. (2007) echoed this realization, noting that higher frequencies are more sensitive to changes in snowpack stratigraphy at the expense of reduced penetration capabilities; they found that Ku- band was well-suited to extracting stratigraphic information. Layers having undergone melt- refreeze conditions tend to produce higher backscatter than dry layers because the grains have experienced growth in the presence of melt water (Strozzi & Mätzler, 1998). Yueh et al. (2009) found the presence of ice lenses within the snowpack to increase backscatter but noted that ice layers much thinner than the incident wavelength may not be visible to the radar. Radar is limited in its capability to distinguish snowpack stratigraphy where subtle transitions in dielectric properties exist across layers.

Substrate

Substrate, in this study, refers to the soil existing beneath the snowpack. Vegetation will also be discussed under this heading although it exists not only beneath the snowpack but also throughout it in many cases.

Vegetation can affect the radar response through the size of its constituent parts, its orientation and its density. In the microwave region the size of components such as stems, leaves and fruit are large relative to incident λ and so it is considered an inhomogeneous, anistotropic medium (Ulaby & Long, 2014). Vegetation with a predominant structural orientation, such as vertical wheat stalks, can lead to stronger returns for similarly polarized waves whereas vegetation lacking a predominant structure can result in less contrast between

vertically and horizontally polarized radar returns indicating depolarization (Woodhouse, 2006). Depolarization often increases with increasing vegetation density.

There is little agreement on whether the predominant scattering mechanism of vegetation is a surface or volume scattering effect and it has been modelled in numerous ways: as a collection of cylinders (Peake, 1959), as a homogeneous dielectric slab (Bush & Ulaby, 1976), and as clouds of water droplets (Attema & Ulaby, 1978). However there is agreement that vegetation attenuation increases with frequency, especially at off-nadir angles (Ulaby et al., 1976). In dense crop canopies such as alfalfa, the scattering contribution from the underlying soil was found to be minimal in the 8-18 GHz range (Ulaby et al., 1975). When electromagnetic waves can penetrate through the canopy, the periodic undulation of the soil common to row crops can lead to coherent effects similar to Bragg scattering (Woodhouse, 2006).

Soil is a dielectric mixture of air, soil particles, and bound and free water (Ulaby & Long, 2014). The scattering properties of soil are driven largely by its water content which impacts its dielectric properties (Ulaby et al., 1986). In dry soil, $\varepsilon' \approx 4$ and the radar response is driven by volume scattering. Waves are able to penetrate the soil to a frequency-dependent depth; backscatter is typically lower for dry soils (Wegmüller, 1990). Increasing the amount of water in the soil causes an increase in ε'. This reduces penetration and changes the dominant scattering mechanism to surface scattering, controlled by surface roughness. Freezing the soil has the opposite effect, causing ε' to fall to values similar to that of dry soils (Wegmüller, 1990); thus there exists a high contrast between the radar response of frozen and thawed soil whereby frozen soils exhibit a weaker response.

2.4 Scattering mechanisms

Radar interaction with a snowpack can be described in terms of two general types of scattering: surface and volume. As discussed in section 2.3.3, surface scattering is heavily dependent on the scale of surface features relative to the incident wavelength and can range from specular to diffuse as roughness increases. Within a snowpack, it can occur at the air-snow interface, the snow-ground interface and at the interfaces between layers of snow with contrasting ε'. In a dry snowpack, surface scattering from the air-snow interface and internal layers is negligible due to a small difference in ε' across the boundaries and can therefore be ignored (Ulaby et al., 1982). Volume scattering is generally considered to be isotropic, scattering equally in all directions (Woodhouse, 2006). It occurs through an interaction with ice crystals in an air background within the snow volume (Ulaby et al., 1984). Rott et al. (2010) explains that the total backscatter from a snowpack (σ_t) is a summation of scattering mechanisms as shown:

$$\sigma_t = \sigma_{as} + \sigma_v + \sigma_{gv} + \sigma_g \tag{2.19}$$

where (σ_{as}) is scattering at the air-snow interface, (σ_v) is scattering from the snow volume, (σ_{gv}) is scattering from the ground surface and snow volume, and (σ_g) is scattering from the ground surface. These interactions are controlled by both wave and target parameters (Ulaby et al., 1984). **Figure 2.7** illustrates this concept for a simple two-layer snowpack.

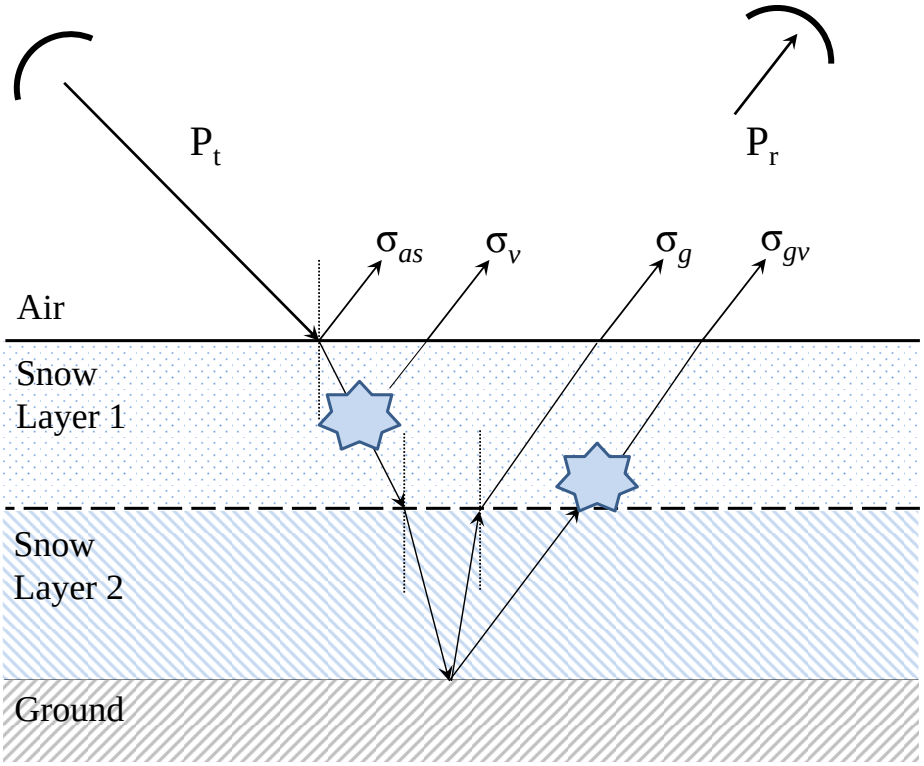

Figure 2.7 Scattering mechanisms of radar interaction with a two-layer snowpack over ground (Adapted from Rott et al., 2010). P_t and P_r represent power transmitted and signal received. A bistatic radar configuration is shown for clarity.

In a dry snowpack, volume scattering dominates the radar response especially at off-nadir incidence angles (Ulaby et al., 1986). The magnitude of this response is driven by the ratio of particle size to incident λ, under the assumption of spherical grain shape (Woodhouse, 2006). Based on this assumption one of two models may be used to approximate the scattering of microwaves from a snowpack volume, depending on λ of the incident wave and size of the snow grains under observation. The Rayleigh scattering model can be used when ice particles are much smaller than the incident wavelength (Ulaby et al., 1981). Under this model, the scattering cross section is strongly dependent on the size of the scatterer and the wavelength, increasing rapidly with both (Mätzler, 1987). The Mie scattering model is used as grain size approaches λ. Scattering under this model varies periodically due to patterns of constructive and destructive interference and is sensitive to small changes in grain size (Woodhouse, 2006). The occurrence

of constructive interference can therefore lead to a scattering cross section much larger than the particle size.

2.5 Modelling with MEMLS-Active

The use of electromagnetic models coupled with observational data provides a means by which we can address and understand the interaction between microwaves and the snow volume. The Microwave Emission Model of Layered Snowpacks (MEMLS) of Wiesmann and Mätzler (1999) is one such model. In this thesis, the third edition of the model, adapted for active microwave applications (MEMLS3-A), will be used to simulate simplified snowpack conditions in order to demonstrate and strengthen our understanding of snowpack interactions with microwaves in support of the results.

MEMLS is based on radiative transfer theory and uses six-flux theory to describe scattering and absorption where two fluxes provide vertical movement in the ± Z direction and four fluxes provide movement in the ± X and Y direction as shown in **Figure 2.8**. MEMLS was initially developed for passive microwave observations in the 5 – 100 GHz range but has been recently adapted for active microwave in its third edition (MEMLS3-A) (Proksch et al., 2015b). Kirchoff's law provides the link between active and passive microwave, through reflectivity (r) and emissivity (e), which allows MEMLS3-A to model backscatter whereby:

$$r = 1 - e \tag{2.20}$$

Earlier electromagnetic snow models tended to simplify the snowpack to one layer for the sake of efficient computing and a reduction in complexity (Proksch et al., 2015b). Later, more realistic models were based on dense media radiative transfer theory (DMRT) but these models require more complex microstructural input parameters that can only be measured using

microcomputed tomography (μCT) and are therefore less feasible to use (Proksch et al., 2015b). MEMLS requires exponential correlation length (p_{ex}) as a microstructural input which can be obtained from objective and efficient field measurements. Ongoing studies are investigating the use of the SnowMicroPen (SMP) instead of μCT to measure p_{ex} (Proksch et al, 2015a).

The snowcover in MEMLS3-A is represented as a stack of horizontal layers with planar boundaries between each layer and also at the air-snow interface; the snow-ground interface is specified by its reflectivity (s_o). A sandwich model combines the interactions at the layer interfaces (Weismann & Mätzler, 1999). Layers are characterized by thickness, correlation length, density, salinity, liquid water content, and temperature. **Figure 2.8** conceptualizes the model.

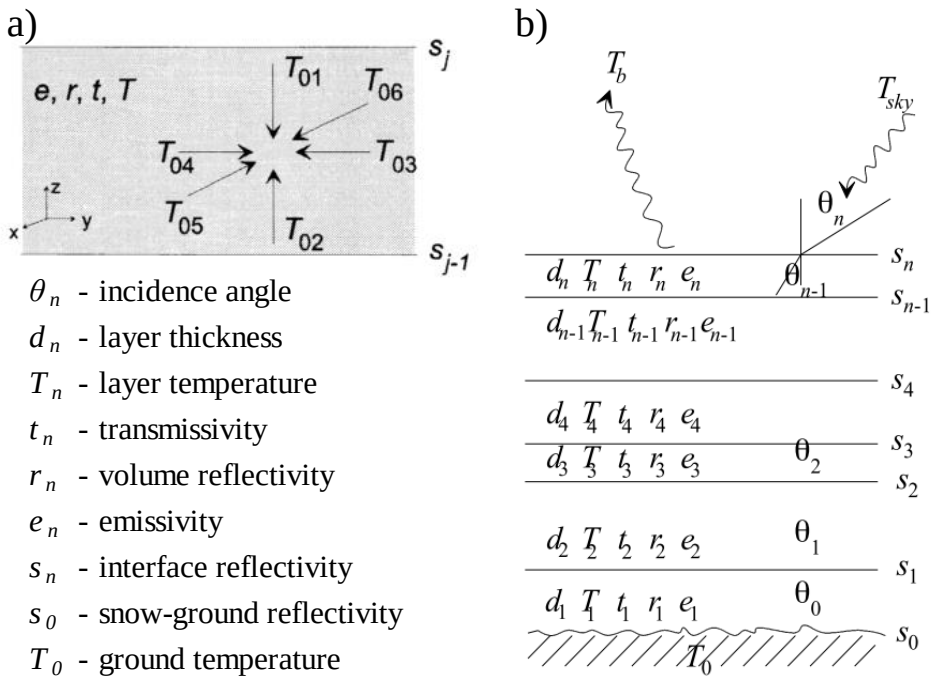

Figure 2.8 Conceptualization of MEMLS3-A. Six-flux schematic showing flux directions T_{01} to T_{06} (a). Layered structure and inputs for an n-layer snowpack (b). Adapted from Wiesmann & Mätzler (1999).

Reflectivity (r) describes the radiation scattered in a hemisphere above the surface and can be estimated in terms of specular (r_s) and diffuse (r_d) components where $r = r_d + r_s$ (Proksch et al., 2015b). Likewise, diffuse (σ^o_d) and specular backscatter (σ^o_s) are calculated separately and summed to yield total backscatter. Where μ_n is defined as the cosine of the incidence angle, the diffuse backscatter is determined by:

$$\sigma_d^o = 4r_d\mu_n^2 \tag{2.21}$$

Diffuse backscatter must be further specified for its co- and cross-polarized state, determined by the splitting parameter (q) which defines the cross-polarized proportion (Proksch et al., 2015b). Given that p and p' provide the incident and scattered polarization σ_{dv} and σ_{dh} are calculated as follows:

$$\sigma^o_{d,pp'} = \begin{cases} (1-q)\sigma^o_{d,v}, & p = p' = v \\ (1-q)\sigma^o_{d,h}, & p = p' = h \\ \frac{q(\sigma^o_{d,v}+\sigma^o_{d,h})}{2}, & p = v, p' = h; or\ p = h, p' = v \end{cases} \tag{2.22}$$

This simplifies to:

$$\sigma^o_{d,v} = \sigma^o_{d,vv} + \sigma^o_{d,hv} = 4r_{d,v}\mu_n^2 \tag{2.23}$$

$$\sigma^o_{d,h} = \sigma^o_{d,hh} + \sigma^o_{d,vh} = 4r_{dh}\mu_n^2 \tag{2.24}$$

Incorporating the mean-square of surface slope (m^2), specular reflectivity at normal incidence ($r_{s,0}$), and the zenith angle (θ_n), σ^o_s is calculated as follows:

$$\sigma_s^o = r_{s,0}\frac{exp[-tan^2\theta_n/(2m^2)]}{2m^2u_n^4} \tag{2.25}$$

The total backscatter is then calculated as the sum of σ^o_d and σ^o_s.

MEMLS3-A was validated with observations from Sodankyla, Finland at 10.2, 13.3 and 16.7 GHz using a 50° incidence angle. Observed SWE for this validation ranged from 135 – 160 mm, with an average density of 190 kg m^{-3} and an SMP-derived p_{ex} ranging from 0.163 to 0.194 mm (Lemmetyinen et al., 2013). Vegetation over 10 cm in height had been removed from the site leaving only surface vegetation consisting of lichen, moss and heather (Proksch et al., 2015b).

Limitations of MEMLS3-A arise due to its balance between efficiency and complexity: The model works under the assumption of spherical snow grains and therefore does not consider shape, aggregation of grains or other microstructural characteristics. The value of q is empirically derived and does not account for the scattering efficiency of snow. Also, soil scattering is parameterized only with s_o and T_0, ignoring other soil characteristics (Proksch et al., 2015b). Furthermore there is currently no mechanism for parameterizing ice layers within the model. Montpetit et al. (2013) used very dense snow layers (917 kg m^{-2}) in place of ice although they acknowledge that a dense snow layer will scatter microwaves whereas pure ice will absorb and reflect microwaves without scattering. Finally, there is no way to account for presence of vegetation within and beneath the snowpack.

Chapter 3 Ku- and X-band radar observations of deep seasonal snow in agricultural fields in Ontario

3.1 Overview

Recent studies of active microwave response to shallow to moderate snow depth have been conducted in sub-Arctic and mountain environments but less so over seasonal mid-latitude snow. Twenty-six radar observations of snow at Ku- and X-band were made in hay fields near Maryhill, Ontario during the 2013-14 winter season and extended for the 2014-15 season to include sites in Englehart, Ontario. The bare ground was scanned during early season snow-free conditions where possible or through complete snow excavation within the radar's field of view. The natural snowpack was scanned throughout the season as snow accumulated; a range of snow water equivalent (SWE) from 0-186 mm was observed. *In situ* measurements of the snowpack properties accompanied the radar observations. Ku-band showed sensitivity to snow accumulation whereby backscatter increased with SWE up to 140 mm beyond which reduced sensitivity was observed. X-band did not show sensitivity to SWE. An investigation of the seasonal depth hoar evolution revealed sensitivity to grain growth at both frequencies. The Microwave Emission Model of Layered Snowpacks (MEMLS3-A) in active microwave configuration confirmed this behaviour. Early season backscatter signatures from low-accumulation snowpack conditions were influenced predominately by vegetation present in the fields as indicated by the polarimetric response. As the snow accumulation increased, the vegetation influence decreased and the snowpack controlled the radar response.

3.2 Introduction

Snow is an important component of the annual terrestrial water cycle. Characterizing and quantifying snow state is important given its role in water resource management and energy budget modeling (Brown & Mote, 2009; Callaghan et al., 2011). Run-off from snow melt provides fresh water for aquatic ecosystems, agriculture, industry, and municipal water supply (Pomeroy et al., 2009). Furthermore, long-term snow mapping studies provide insights into the nature of snow as an indicator of climate change (Brown & Mote, 2009). Given its importance, changes in snow extent, duration, and distribution due to climate change have emphasized the need for a practical system of monitoring (WMO, 1997). This has prompted organizations such as the World Meteorological Organization and the Integrated Global Observing Strategy to articulate the need for high-resolution snow water equivalent observations (IGOS, 2007).

Remote sensing of snow using radar observations can be a practical means of obtaining information on seasonal snowpack accumulation at high spatial and temporal resolution (Rott et al., 2010). Recent studies have identified microwave frequencies in the range of 8-18 GHz as being sensitive to volumetric snow properties (King et al., 2013; Yueh et al., 2009). At these frequencies, penetration depth of radar waves into dry snow is estimated to be greater than 1 m (Mätzler, 1987). Research in the European Alps, American Rocky mountains, sub-Arctic Scandinavia and Canada have demonstrated a strong relationship between Ku-band scatterometer observations and SWE. Specifically co-polarized vertical Ku-band backscatter was observed to increase by 0.15-0.5 dB for every 1 cm of SWE accumulation in the Colorado Rocky mountains, and by 0.82 dB per cm in the Canadian subarctic (King et al., 2015; Yueh et al., 2009). However there are limited empirical studies exploring the usefulness of Ku- and X-band frequencies for observing seasonal snow in a typical mid-latitude continental climate agricultural

region. In addition, it is not clear what the role of snowpack stratigraphy, especially large grain size layers such as depth hoar, might be on the backscatter response from snow in this region; the role of agricultural vegetation on the radar signal is also unclear. Air temperature fluctuation and variation in the state of precipitation inputs throughout the winter combined with greater accumulation can result in a highly complex snowpack with multiple crust, melt-refreeze, and freezing rain layers. The Ontario snow accumulation environment is therefore well-suited to probe the operational range of these frequencies and to understand their limitations.

The aim of this research is to explore the radar response from seasonal snow that accumulated during the winter seasons of 2013-14 and 2014-15 in Maryhill, Ontario and Englehart, Ontario. It was designed as a case study primarily to investigate the electromagnetic response of Ku- and X-band radar to a range of snow depths and snow properties not considered in other studies, over two winters in Ontario. A comprehensive dataset of polarimetric ground-based active microwave measurements were collected. Co-located, *in situ* measurements of the snow and underlying soil were also made to interpret the scatterometer measurements. The objective of the project was to explain the backscatter response of Ku- and X-band scatterometer signals from snow in agricultural fields through completion of three specific goals: 1) to quantify and characterize the active microwave response over an expanded range of depths of seasonal snow at 9.6 and 17.2 GHz frequencies, 2) explain the polarimetric response in this environment, and 3) develop a field data set to test microwave scattering models for snow accumulation in an agricultural field.

3.3 Study sites

The study sites for this experiment were located in Maryhill and Englehart, Ontario and (**Figure 3.1**). Maryhill (80°22'47.62"W, 43°32'55.27"N) is situated at about 317 m above sea level (ASL) and on average receives nearly 160 cm of snowfall annually (Environment Canada, 2015).

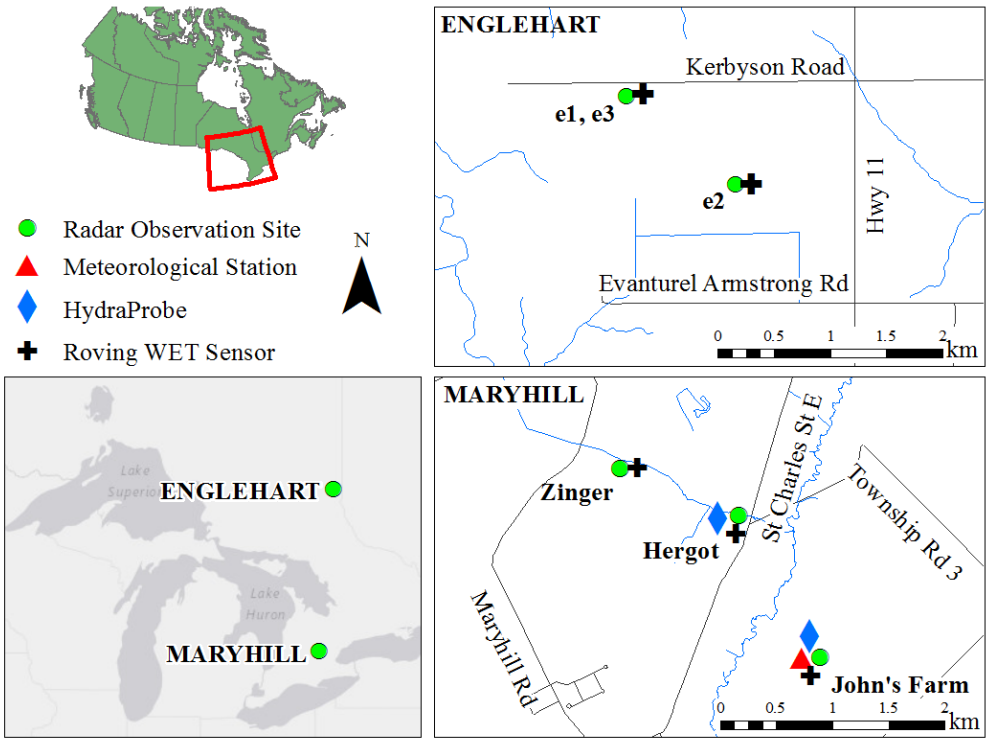

Figure 3.1 Study site locations in Maryhill and Englehart, Ontario (DMTI, 2014; ESRI 2014; Regional Municipality of Waterloo, 2014).

The soil in this region is a well-drained gravelly to sandy loam (Presant & Wicklund, 1971). Englehart (79°50'49.02"W, 47°46'6.38"N) is situated at about 243 m ASL and receives over 222 cm of snowfall annually (Environment Canada, 2015). The soil in this region is classified as a well-drained silty loam (Hoffman et al., 1972). Thirty-year winter climate normals (1981-2010) for both regions are provided in **Table 3.1**.

Table 3.1 Study region climate normal for Maryhill and Englehart (Environment Canada, 2015).

	Maryhill				Englehart			
	Dec	Jan	Feb	Mar	Dec	Jan	Feb	Mar
Daily Average (°C)	-3.3	-6.5	-5.5	-1	-10.9	-16.2	-13.3	-6.7
Daily Minimum (°C)	-6.8	-10.3	-9.7	-5.6	-16	-22.4	-20.1	-12.9
Daily Maximum (°C)	0.2	-2.6	-1.2	3.6	-5.8	-10	-6.5	-0.5

During the 2013-14 season, the study site was located in a cut hay field near Maryhill, Ontario. The ground was level with furrows of approximately 5 cm depth and 55 cm spacing arranged in an east-west orientation. Between January and March, 2014, the study area was visited on four occasions and each time, a new location within the field was chosen based on variation in snow depth.

Three separate fields in Maryhill were revisited during the 2014-15 season. The first field, named the Zinger site (80°23'20.87"W 43°33'4.96"N), was a bare field with sparse vegetation; surface features appeared randomly distributed and rows were not visible. The second site, named the Hergot site (80°22'47.62"W 43°32'55.24"N) was a densely vegetated hay field with a crop height of approximately 50 cm; rows were not visible and the vegetation was sufficiently dense that the underlying ground could not be seen with the eye. The third site, named John's farm site (80°22'30.48"W 43°32'25.38"N) was similar to the Hergot site in terms of the vegetation, however bare ground was visible beneath the vegetation. Photographs of the sites pre-snow accumulation are shown in **Figure 3.2**.

In order to observe deeper snow, the study area was expanded to include the Englehart sites, in February 2015. Three sites were chosen within the same hay field based on variation in snow depth; the hay had been cut and the remaining crop stubble was less than 15 cm in height.

Figure 3.2 Maryhill field sites on Dec 2, 2014: Zinger site (left), Hergot site (centre), and John's farm site (right).

3.4 Data and methods

3.4.1 Background

The interaction between radar and snow can be subdivided into four unique scattering mechanisms. The total backscatter (σ_t) from a snowpack on the ground can be found through summation of surface scattering at the air-snow interface (σ_{as}), volume scattering within the snowpack (σ_v), ground surface scattering (σ_g), and ground-volume scattering (σ_{gv}) (Rott et al 2010). **Figure 3.3** illustrates this concept with a simple single-layer snowpack. The contribution of each mechanism to σ_t depends on the combination of snowpack parameters, substrate parameters, and sensor parameters (Shi & Dozier, 2000).

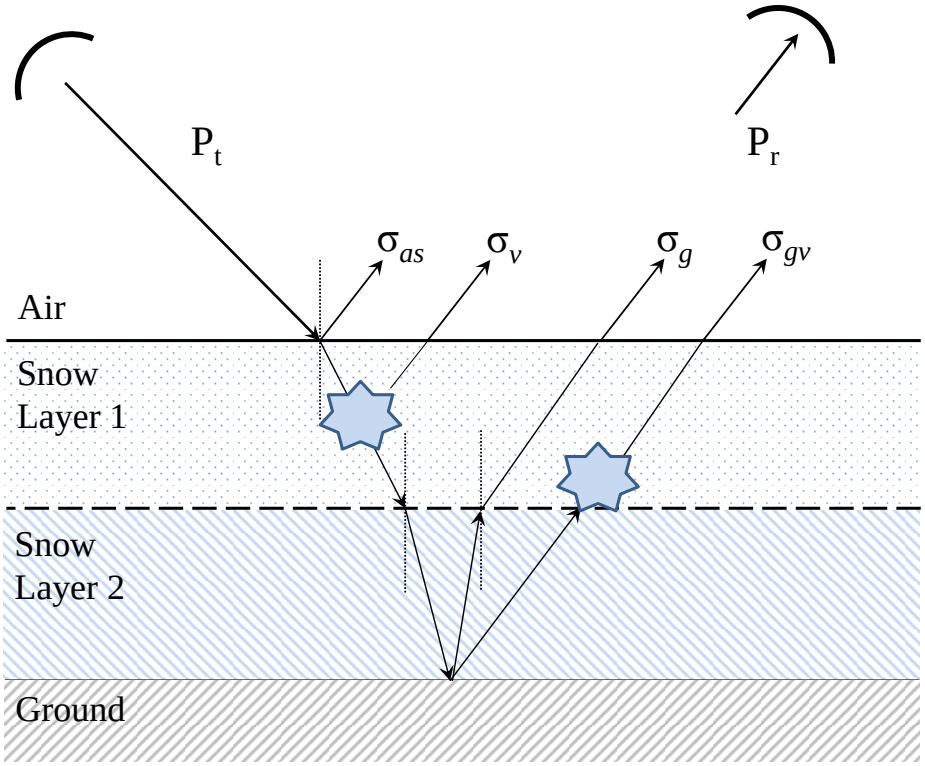

Figure 3.3 Radar scattering mechanisms within a snowpack (Modified from Rott et al. 2010).

3.4.2 Snowpack parameters

Critical snowpack parameters are those which have a strong influence on radar backscatter, and include complex relative permittivity, density, and stratigraphy. The real portion (*ε'*) of the complex relative permittivity describes the ability of a material to store energy and conduct electricity (King et al., 2015). A strong radar return may be created at discontinuities in *ε'*, as the electromagnetic energy passes from one material to another, characterized by a marked difference in ε' such as through wet and dry layers in a snowpack (Marshall et al., 2007). The variation of ε' along a given path will determine the depth of penetration of the radar, and how much information can be extracted from the signal (Ulaby et al., 1984). Snow is considered a dielectric mixture of its constituents, ice, air, and at times, liquid water (*ε'*= 3.17, 1, and 80, respectively) and therefore *ε'* of snow is a function of this combination (Colbeck, 1982b; Hallikainen et al., 1986, Ulaby et al., 1984). Density, which is a

measure of the amount of mass within a given volume, is also therefore controlled by the proportion of these constituents. In dry snow, primarily observed in this study, density controls ε' and for densities of 200-500 kg m^{-3}, ε' will range from about 1.4-2 (Tiuri et al., 1984; Ulaby et al., 1984). The following relationship relates the density of dry snow (ρ_d) to ε' (Tiuri et al., 1984):

$$\varepsilon' = 1 + 2\rho_d \tag{3.1}$$

Snow grain metamorphosis can impact density as grains and grain structure change in time. Snowpack densification can be caused by wind slab development which occurs when wind exposure causes snow grains to fracture and become rounded and therefore able to pack tightly (Fierz et al., 2009). Densities of wind slab can range from 350 kg m^{-3} to beyond 500 kg m^{-3} (Benson & Sturm, 1993). King et al. (2015) reported depth hoar layers within a subarctic snowpack to have a density of 170 kg m^{-3} while Fierz et al. (2009) described fresh snow with a density of 100 kg m^{-3}. Densities within a snowpack can also be affected by compaction as weight from added accumulation can compresses basal snow layers (Bormann et al., 2013; Langlois et al., 2007). Changes in snow grain structure may change density and therefore impact the radar return by modifying the ε' of the snowpack through the relationship expressed in (3.1).

Throughout the season, complex stratigraphy can develop within a snowpack caused by successive snowfall events, freezing rain, and metamorphosis; this is especially true for mid-latitude continental snowpacks. Unlike the single-layer snowpack in **Figure 3.3**, natural snowpacks in this environment typically feature multiple layers each with their own characteristics (Sturm et al., 1995); the scattering mechanisms listed above act in concert within each layer. Discontinuity of ε' between ice and snow layers present within the snowpack can increase backscatter and reduce the penetration of waves with frequencies of relatively shorter

wavelengths (Marshall & Koh, 2008; Yueh et al., 2009). Similarly, Marshall et al. (2007) noted that higher frequencies were more sensitive to changes in snowpack stratigraphy at the expense of reduced penetration capabilities and overall they indicated Ku-band was well-suited to extracting stratigraphic information. However the study by Marshall et al. (2007) was performed at nadir which means the microwaves were subject to less reflection than that which was expected in this study and therefore had greater penetration capabilities and was influenced more strongly by the stratigraphy. From this it becomes evident however, that in the absence of a substantial difference in geometric and dielectric properties between layers, radar cannot distinguish the stratigraphy of the pack. However, within a complex snowpack, layers with substantially different ε' can cause an increase in the σ_s component of σ_t between layers within the snowpack where internal reflections may occur (Du et al., 2010). Grain size and shape characteristics within a given layer can influence σ_v and σ_{gv}. Specifically, larger grains are thought to enhance higher-order scattering (Du et al., 2010; King et al., 2013). Strozzi & Mätzler (1998) found this occurred in melt-refreeze layers which experienced grain growth in the presence of melt water at 35 GHz. Similarily, King et al. (2013 & 2015) suggested that vertical orientation combined with the larger size of depth hoar grains contributed to an elevated vertically-polarized response at Ku-band frequencies. Although wet snow was generally not encountered in this study, the presence of water in the snowpack even at low concentrations (0.5% by volume) affects the magnitude of the relative permittivity such that penetration depth of a radar wave within the snowpack is severely limited (Ulaby et al., 1982).

3.4.3 Substrate parameters

Soil beneath the snowpack can contribute to σ_t through σ_g and σ_{gv} interaction at the snow-soil interface where the incident wave can penetrate the snowpack. The magnitude of this interaction is controlled primarily by dielectric properties of the soil related to the volume of free water present (Ulaby et al., 1986). Since soil is considered a dielectric mixture of soil particles, air, free water, and bound water, ε' of soil is heavily influenced by ε' of water when present. In dry soil conditions, incident waves can penetrate the soil volume and the predominant scattering mechanism is volume scattering, leading to a lower power return (Richards, 2009). When soils are wet, penetration of the waves is severely limited due to the increase in ε', and the radar response originates at the soil surface, driven by surface roughness. For soils in which the surface is smooth, as governed by the Fraunhoffer criteria, specular reflection dominates whereas scattering becomes increasingly diffuse with increasing roughness. Freezing the soil decreases ε' to levels similar to dry soil, decreasing backscatter and causing a sharp contrast between the radar response of frozen and thawed soil frozen soils (Wegmüller, 1990).

Vegetation within and beneath the snowpack can also impact scattering of the incident wave through the size of its constituent parts relative to the incident wavelength, its orientation and the density. This includes crop residue which can strongly affect radar backscatter (McNairn et al., 2002). Scattering from vegetation is typically dominated by volume scattering since there are no distinct air-vegetation boundaries (Ulaby et al., 1982). However within vegetation canopies, including senesced crop canopies, multiple scattering mechanisms exist: leaves and inclined stems can yield multiple bounce and volume scattering while vertical stalks typically yield double-bounce scattering (McNairn et al., 2002). The orientation of predominant vegetation features can lead to preferential scattering from similarly polarized waves whereas the

lack of a preferential structure can decrease the contrast between vertical and horizontal returns and increase depolarization especially when coupled with an increase in density (Woodhouse, 2006). Evans et al. (1988) also linked depolarization with vegetation density. Ulaby et al. (1975) determined that the scattering contribution, in the 8 – 18 GHz range, from the soil beneath a high-density, mature alfalfa crop was minimal. Vegetation attenuation also tends to increase with incident-wave frequency especially at off-nadir angles (Ulaby et al., 1976).

3.4.4 System parameters

Radar measurements were made using the University of Waterloo scatterometer (UW-Scat) which is a fully polarimetric, frequency-modulated continuous-wave system that operates at centre frequencies of 17.2 and 9.6 GHz (King et al, 2013). It is a portable ground-based system that allows for rapid deployment in the field. A two-axis positioner allows the system to rotate 360° in azimuth and from 15° to 105° in elevation. The scan geometry employed in this study included 40° azimuth sweeps through 28° of elevation in 3° increments from 34° to 59°. Azimuth sweeps were averaged to produce a normalized radar cross section (NRCS) value for each scan elevation. Radar calibration efforts were made on-site with an in-scene trihedral corner reflector combined with a sky measurement that was coherently subtracted from range profiles to account for system noise. Errors inherent in UW-Scat measurements were estimated at ±2.0 dB for both frequencies, and include a 0.5 dB allowance for random error (King et al., 2015). **Table 3.2** summarizes the operating parameters of UW-Scat. A detailed description of the equipment, including its calibration procedures, can be found in King et al. (2013).

Table 3.2 UW-Scat operating parameters.

Parameter	Ku	X
RF output frequency (GHz)	16.95-17.45	9.35-9.85
Centre frequency (GHz)	17.2	9.6
Transmit power, narrow beam (dBm)	-8	-11.8
Transmit bandwidth (MHz)	500	500
Range Resolution (m)	0.3	0.3
Antenna beamwidth, narrow beam (°)	5.6	4.3
Cross-polarization isolation (dB)	>30	>30
Transmit/receive polarizations (linear)	VV, HH, VH, HV	VV, HH, VH, HV
Sensitivity (dB m^2m^{-2})	-50	-50

UW-Scat sends linearly polarized waves of vertical and horizontal orientation, and receives any combination of vertically and horizontally polarized waves. The polarization state of an electromagnetic wave, and the theoretical polarization ellipse, can be completely described in terms of its ellipticity (χ) and orientation angles (ψ). The range of χ and ψ, from -45° to 45° and 0° to 180° respectively, describe all possible polarization states (Evans et al., 1988; Zebker et al., 1987). Note that in some cases the range of ψ may be alternatively expressed as -90° to 90° with the same meaning. The shape of the polarization ellipse is governed by χ and is 0° for linear polarization, when only one component (vertical or horizontal) of the electrical field exists, and ± 45° for circular polarization, when the magnitudes of the vertical and horizontal components are equal (Ulaby et al., 1981). For any other value of χ, the polarization is said to be elliptical (Ulaby & Long, 2014). The orientation of the ellipse and the direction of its major axis is governed by ψ which indicates, for the linear case, vertical polarization when ψ= 90° and horizontal polarization when ψ= 0° and 180° (Evans et al., 1988; Zebker et al., 1987). If the orientation of an incident wave is parallel to the dominant plane of a target, along with an expectation of first-order scattering such as σ_s or σ_g, this can enhance the co-polarized backscatter. Conversely depolarization, which occurs when the polarization state of an incident

wave is changed through an interaction with a target, can result from multiple-scattering often occurring from σ_v and σ_{gv} interactions. According to Du et al. (2010) snow grain size and shape play a strong role in multiple-scattering and therefore depolarization. Dense vegetation can also play a role as a strong depolarizing target (McNairn et al., 2002).

In order to visualize the polarimetric response of a target, two tools may be utilized: The polarization signature and instantaneous polarization-state histogram are 3-dimensional plots which graphically represent the polarization state of the received wave in terms of ψ and χ. The polarization signature displays χ, ψ, and the relative NRCS as the x, y and z axes respectively, and allows us to visualize the power returned to the antenna as a function of send and receive polarizations (Evans et al., 1988). A co-polarized signature illustrates the case where transmit and receive polarizations are equal while the cross-polarized signature illustrates the case where transmit and receive polarizations are orthogonal. The relative NRCS is normalized to 1. Peaks in the graph indicate polarizations that yield maximum received power and troughs occur for polarizations associated with a minimal return power; the overall shape suggests the scattering mechanism. The minimum NRCS value is known as the pedestal height and can be caused by multiple scattering from a depolarizing scatterer in-scene, averaging of multiple samples with dissimilar scatterers, and system noise (Evans et al, 1988). Examples of co-polarized signatures for three types of scattering are shown in **Figure 3.4**: isotropic scattering from a sphere (left), Bragg scattering (centre), and double-bounce scattering (right).

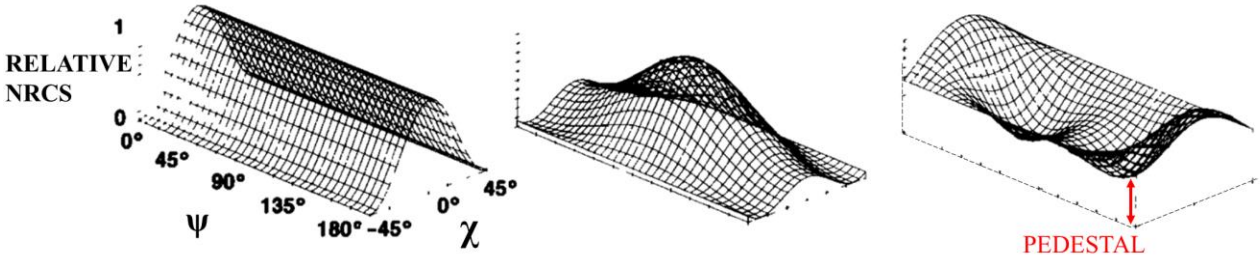

Figure 3.4 Co-polarized signatures for an isotropically scattering sphere (left), Bragg scattering (centre), and a dihedral corner reflector showing double bounce scattering (right). Pedestal indicated on right-most plot for clarity. Figure modified from Zebker et al. (1987).

The instantaneous polarization-state histogram shows the aggregated polarization state of scattered waves across all azimuth angles and range bins, for a known incident vertical or horizontal polarization. The histogram has the same X-Y basis as the polarization signature but it has a count of the state of the returned waves on the z-axis. The z-axis of the histogram is not fixed and is allowed to float thereby ensuring that the shape and spread of the histogram can be seen; the magnitude of the peaks is less important than the shape and spread. The pattern and degree to which the histogram is peaked or spread over the range of χ or ψ, indicates the dominant received polarization state and thus the degree of depolarization. Examples of three different cases are provided in **Figure 3.5**. On the left is a histogram of the received state from vertical-transmit energy indicating that the scattered wave polarization has relatively little depolarization; the well-defined peak is centred in the region of the graph corresponding to vertical, linear polarization (χ= 0°, ψ= 0°). The middle figure is a histogram of the received horizontal-transmit energy; two well-defined peaks are located in the region of the graph correspond to horizontal, linearly polarized radiation (χ= 0°, ψ= ±90°). The plot on the right is once again the vertical-transmit energy which shows a response spread over the entire range of χ and ψ, indicating strong target depolarization.

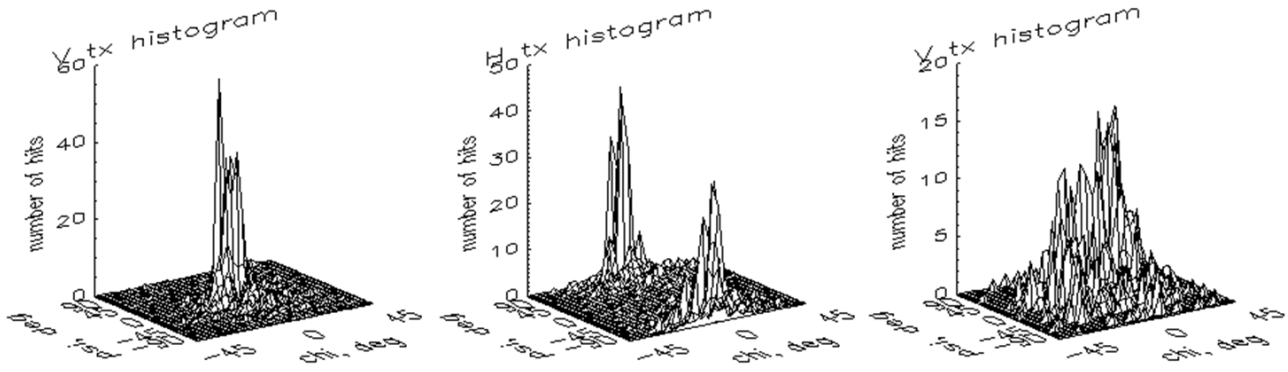

Figure 3.5 Examples of instantaneous polarization-state histograms for vertical incident polarization (left), horizontal incident polarization (centre), and vertical incident polarization showing evidence of depolarization in the scattered wave (right). The incident wave in all cases was linearly polarized.

3.4.5 Field observations

Backscatter measurements were made using a combination of vertical (V) and horizontal (H) send-receive polarization states (VV, HH, and VH). The radar was tripod-mounted, placing the antenna at 2.2 m above the snow surface. Each scan was repeated 3 times and averaged in order to minimize the effects of system noise.

In situ measurements from snow pits included snow depth, density, and temperature measurements along with grain size estimation and stratigraphy observations. A snowpit was dug and snow depth was measured with a ruler along the pit face from the air-snow interface to the exposed ground beneath the snow. To measure snow density, samples were taken from the pit face, starting at the air-snow interface working downward, using a 100 cm^3 cutter. Each sample was weighed on an electric scale and density was then calculated by multiplying the sample mass by the sample volume. Snowpack temperature was measured at 10 cm intervals along the pit face from the air-snow interface to the base of the snowpack using an analog probe thermometer. Readings on the thermometer were allowed to stabilize for two minutes before recording. Snowpack stratigraphy was observed from the pit face by brushing away loose snow

to help expose and distinguish softer layers from harder layers. Layer thickness and position within the snowpack were measured with a ruler and recorded. Photos were taken of the pit face with the ruler in-scene. A gridded comparator card and hand lens were used to make estimates of grain size from snow samples which were gathered from each layer of the snowpack by dislodging snow samples from the pit face with the edge of the comparator card. The samples were viewed under the hand lens and the minimum and maximum extent of the average or most common grain in the sample, were recorded. The sample grain type was recorded as one of the following: rounded, faceted, mixed snow, new snow, or depth hoar. The hardness of the layer was estimated and recorded as finger, pencil, or knife referring to the ability to penetrate the snow layer where finger indicates the softest snow and knife indicates the hardest snow. The grain size estimation procedure was completed three times per snow layer. Note that the maximum extent of the prevailing snow grain measured in this method may be referred to as D_{max} in modelling endeavours. A meteorological station, located 500 m west of the Hergot site in 2013-14 and at John's farm in 2014-15, recorded air temperature, wind speed, relative humidity, and solar radiation at the site; meteorological data for Englehart was sourced from the Earlton-Timiskaming Regional Airport (YXR), located about 7 km southeast of the study site. During the 2014-15 season, two Stevens Hydra Probes (50 MHz) were installed horizontally at depths of 5 cm in the soil at the Hergot site and John's farm which measured soil temperature, moisture content, conductivity, and relative permittivity (real and imaginary components). A Delta-T WET sensor (20 MHz) was used at the Maryhill and Englehart sites to measure soil temperature, permittivity and soil conductivity at several roving locations around each site. During 2013-14 soil temperature data was collected from a Stevens Hydra Probe, installed horizontally at a depth of 5 cm, 500 m west of the Hergot site in an adjacent field; these readings

were assumed to be representative of conditions at the Hergot site. The primary purpose for the use of the Hydra Probes and WET sensor was to determine the timing of soil freeze-up. Weather data for the sites is provided in **Figure 3.6**. In 2013-14, air temperatures exceeded 0°C on January 10, 12 and 13, February 19, 20, and 22, and March 14, 18, 19 and 21. Soil temperatures remained below 0° for the entire observation period in 2013-14. In Maryhill during the 2014-15 season air temperatures were above 0° for much of December and then again on January 3 and 4, January 17 and 18, and briefly (from 15:30 to 17:45) on the afternoon of March 8. Soil temperatures at the Hergot site and John's farm were above 0° for much of December and then remained below 0° from January throughout the remainder of the season. Soil temperature at the Zinger site was not recorded continuously but was measured at 0.2°C on December 2, 2014. It was below 0°C on all subsequent measurements. At the Englehart sites, both air and soil temperatures remained below 0° for the entire observation period.

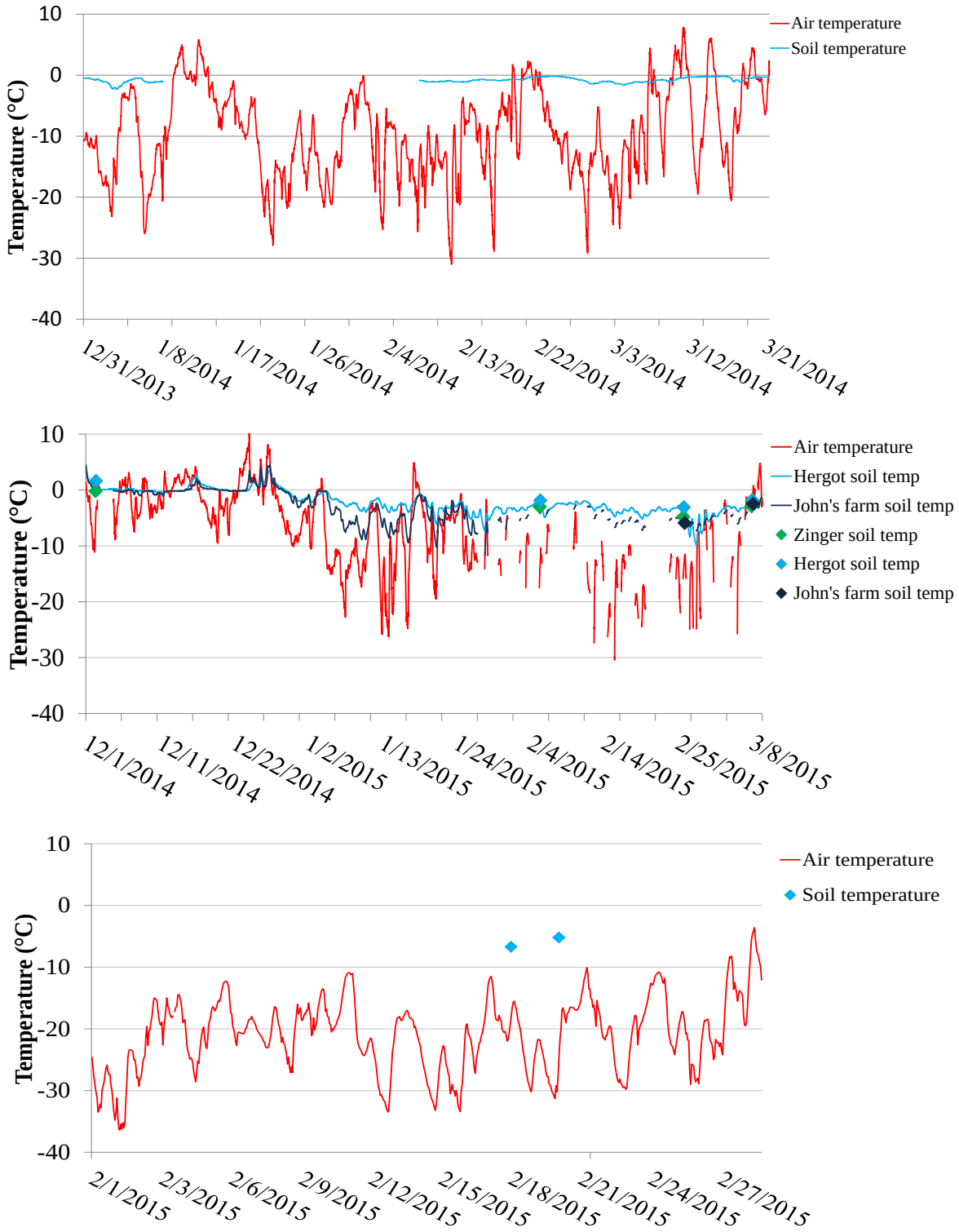

Figure 3.6 Weather data for Maryhill 2013-14 (top), Maryhill 2014-15 (middle), and Englehart 2015 (bottom). Diamond symbols represent roving WET sensor readings. Discontinuous lines indicate periods of equipment failure. Englehart data provided by Environment Canada (2015).

During the 2013-14 season, field observations were collected on January 31, February 2, February 28 and March 21. On each site visit two sets of scans were performed. In the first set of scans, the naturally occurring snowpack was observed at both frequencies. For the second set of scans, all the snow within a 5 m by 5 m area in front of the scatterometer was excavated to bare soil. The excavated area was oriented such that the scatterometer was located at the midpoint of one side facing towards the snow-free area. The scans were repeated for both frequencies using the same parameters and positioning as before. Because the soil temperatures remained below freezing during the study period, the condition of the underlying soil was assumed to have remained constant. For this reason, backscatter measurements for the excavated sites (excluding March 21, 2014) were averaged to represent the snow-free condition. Observations from March 21, 2014 were excluded from this average since snow melt on the surface of the exposed ground resulted in water ponding, a condition that was very different from other excavated sites.

In between the two sets of scans, before the snow was excavated, snow depths were recorded over a 10 m by 10 m area in front of the scatterometer. The measurements were made in a grid with 50 cm spacing, using a Magnaprobe. An exception to this grid spacing was made 2 m directly in front of the scatterometer where a 1 m^2 area was left undisturbed for the snow pit.

In the 2014-15 season, each Maryhill site was scanned prior to snow accumulation on December 2 and then revisited on January 24, January 31, February 5, February 26, and March 8 to observe a range of snow depths. The full suite of *in situ* snowpack observations were made on these dates as well. The Englehart scans were performed in a manner similar to those conducted

in the 2013-14 season whereby the natural snowpack was observed first and then excavated in order to scan the bare ground. The first Englehart site (e1) was observed on February 16, and the second (e2) was observed on February 17; e2 was excavated and the site was re-scanned on February 18. On February 19, the snowpack at e1 was re-scanned, excavated, and then scanned again. A third site (e3) adjacent to e1 was also scanned on February 19; the scan of excavated site e1 served as a proxy to site e3 due to their adjacency and as such e3 was not excavated. *In situ* snowpack observations accompanied the scans at each site.

Soil roughness measurements were made at each Maryhill site in April of 2014 and 2015. Measurements were made in two directions in each case, relative to the range and azimuth direction of the scatterometer position. The range and azimuth directions were generally parallel and perpendicular, respectively, to crop rows where present. Soil roughness measurements were not made in Englehart however from a visual inspection they appeared similar to those observed in Maryhill in 2014-15 and so the study proceeded under the assumption that roughness conditions were similar. In April 2014, soil roughness measurements were made using a piece of sheet steel marked with a 5 cm by 5 cm grid. The steel was inserted orthogonally into the surface of the ground on its long edge just so there were no gaps between the bottom edge of the steel and the soil. Photographs were taken and the relative height of the soil surface against the steel surface was observed and recorded at 5 cm intervals along the length of the steel. This process was completed once in the azimuth direction and once in the range direction. In April 2015, a Leica MS50 Multistation was used to conduct a 3D laser scan (5 mm resolution) at each of the 2014-15 Maryhill sites. Since the scan did not account for multiple returns, the point cloud was manually classified into ground points and non-ground points along three 8 m

transects each in the azimuth and range directions spanning the field of view. RMS roughness values were calculated for each transect and those values in each direction were then averaged.

3.5 Results

3.5.1 Snowpack physical properties

Summary conditions for snow during the observation periods are presented in **Figure 3.7** for the 2014-15 Maryhill time series observations and **Table 3.3** for the 2013-14 and Englehart observations. The maximum snow depth observed in Maryhill was 41 cm, on January 31 and February 28, 2014. The maximum value of SWE observed in Maryhill was 165 mm on February 28, 2014. The maximum thickness of depth hoar within a snowpack in Maryhill was 26 cm, observed at John's farm on March 8, 2015.

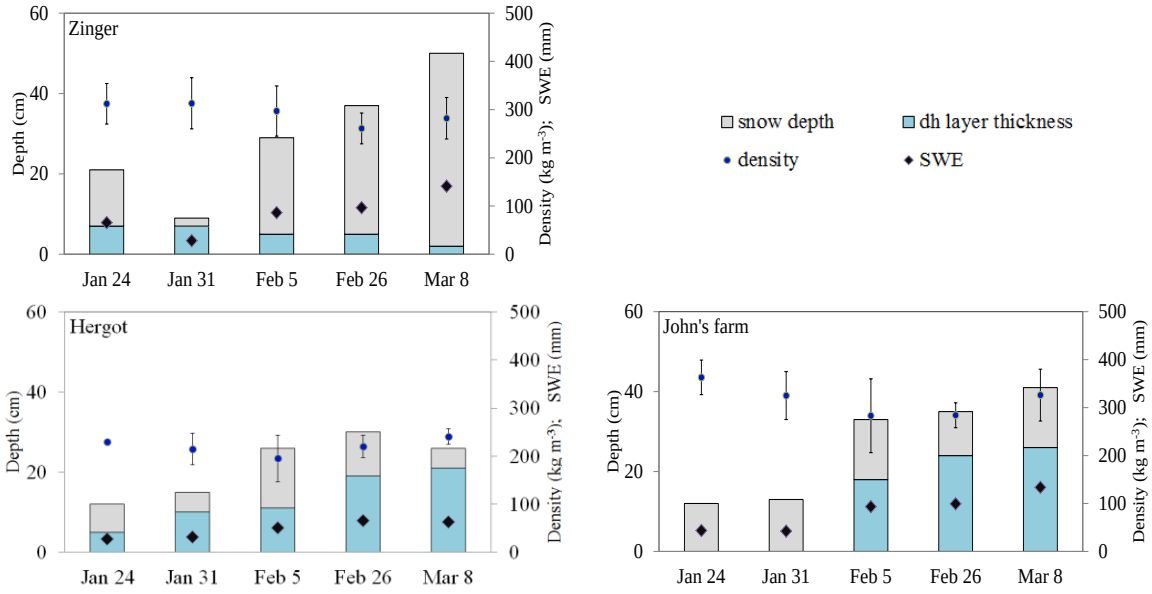

Figure 3.7 Summary of 2014-15 Maryhill time series snowpack conditions. Density error bars represent 1 standard deviation. Depth hoar is abbreviated to dh.

Results for Englehart are presented in tabular format since a time series of observations was not collected. The maximum value of snow depth and SWE observed in Englehart was 67 cm and 186 mm respectively on February 17 at e2. This coincided with the maximum depth hoar thickness within a snowpack of 46 cm. These results were the maximum observed for the entire study.

Table 3.3 Summary of snowpack conditions for the 2013-14 and Englehart sites.

Date	Site	Snow depth (cm)	Depth hoar layer thickness (cm)	Density (kg m^{-3})	SWE (mm)
2013-2014					
31-Jan-2014	NA	41	13	350	144
2-Feb-2014	NA	28	5.5	269	75
28-Feb-2014	NA	41	0	413	165
21-Mar-2014	NA	23	0	456	105
Englehart 2015					
16-Feb-2015	e1	54	37	259	140
17-Feb-2015	e2	67	46	277	186
19-Feb-2015	e1, e3	55	44	263	145

Soil roughness measurements are provided in **Table 3.4**. The Hergot site was the roughest with an average RMS roughness of 4.2 cm. This was caused primarily by the elevated roughness in the Azimuth direction of 6.3 cm which corresponded with the direction of the crop rows. The Zinger site was the next roughest with an overall RMS value of 3.3 cm although there was little evidence of row orientation since RMS roughness was very similar in the range and azimuth direction. John's farm site had a range roughness of 2.2 cm which was similar to that of the Hergot site, but the Azimuth roughness was much less at only 3.2 cm; overall John's farm site exhibited the least roughness with an RMS value of 2.7 cm. These values indicate the soil was electromagnetically rough for all incidence angles according to Fraunhoffer's criteria.

Table 3.4 RMS soil roughness measurements for Maryhill sites in the range and azimuth directions. Average RMS roughness is an average of range and azimuth RMS roughness.

Site	Range (cm)	Azimuth (cm)	Average (cm)
2013/2014	0.8	1.5	1.1
Zinger	3.4	3.2	3.3
Hergot	2.1	6.3	4.2
John's farm	2.2	3.2	2.7

3.5.2 Backscatter response

Comparison between Ku- and X-band backscatter and SWE for all Maryhill observations is shown in **Figure 3.8**. These backscatter observations represent an average of the first three scan lines with incident angles of 35°, 38°, and 41°; whiskers represent minimum and maximum values. The Ku-band observations for the 2013-14 season indicated a sensitivity to SWE for VV and HH polarizations, whereby backscatter increased with SWE. No relationship was apparent for VH polarization. Likewise at X-band there was no apparent relationship as the curve was comparatively flat.

Maryhill observations from the 2014-15 season did not show a clear pattern. The Ku-band observations at the Zinger site revealed little influence of SWE on backscatter. As SWE increased there was negligible change in backscatter response, which remained around -5 dB. The Hergot site observations showed backscatter around 0 dB for levels of SWE around 30 mm while uncharacteristically low levels of backscatter around -12 dB were observed near 60 mm of SWE. Overall there was no discernable relationship between SWE and backscatter at this site. Likewise, at John’s farm, the backscatter showed no clear relationship to SWE. The greatest values of backscatter, above -5 dB, were observed at 60 mm of SWE. The lowest backscatter, near -10 dB, was observed near 140 mm of SWE. At X-band, sensitivity to these levels of SWE appeared minimal at all sites. As observed at Ku-band, abnormally low backscatter around -10 dB was observed at the Hergot site for 60 mm of SWE.

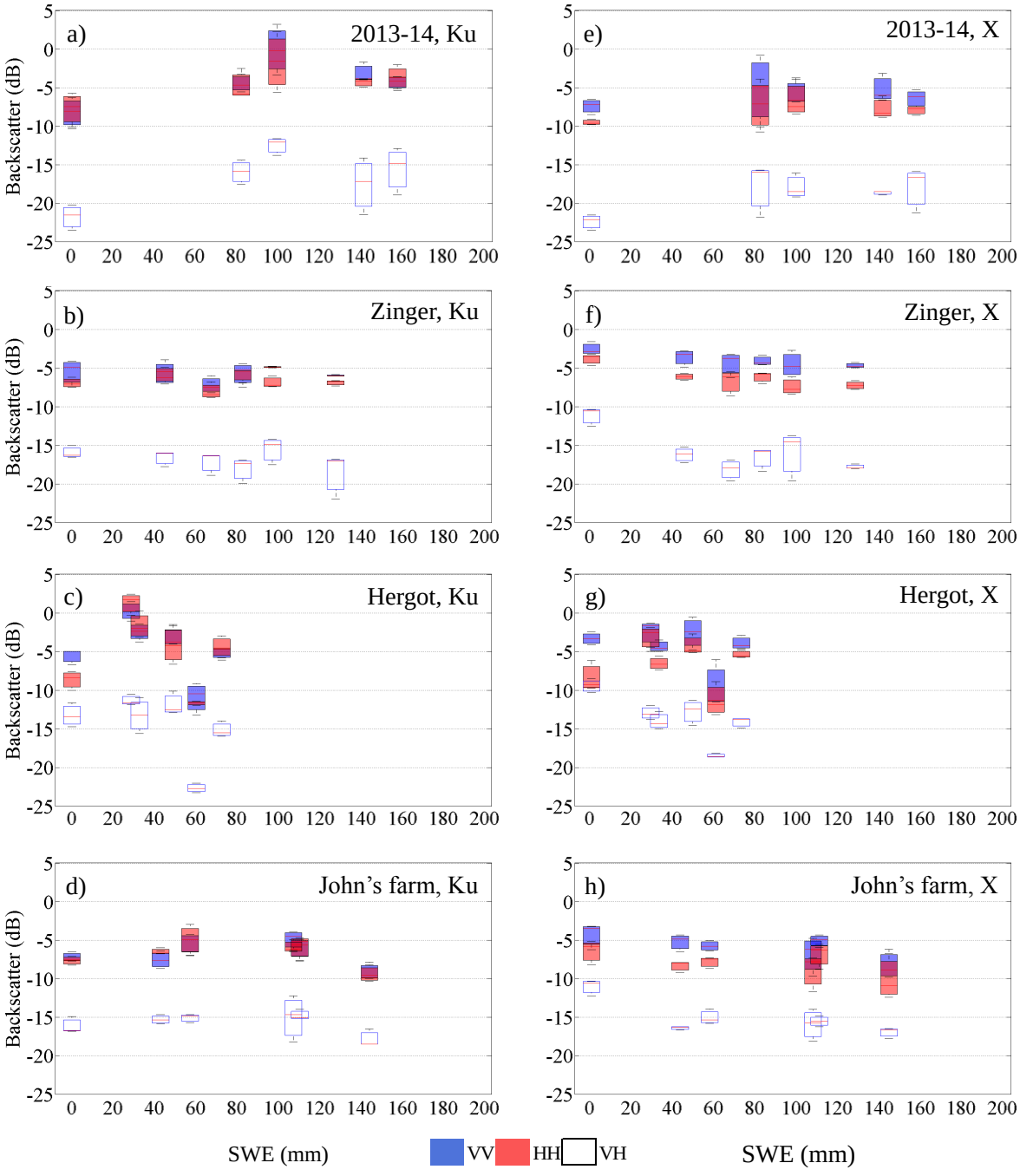

Figure 3.8 Comparison of backscatter and SWE for Maryhill sites. Left-hand column (a-d) shows Ku-band response and right-hand column (e-h) shows X-band response. Observations for 2013-14 are given in a) and e). Observations from 2014-15 are given in b) and f) for the Zinger site, c) and g) for the Hergot site and d) and h) for John's farm site. Dark red indicates overlap between VV and HH backscatter range.

Backscatter and SWE observations for Englehart are provided in **Table 3.5**. No clear relationship with SWE could be observed from these results. The relatively narrow range in backscatter indicated minimal change in response at either frequency for the range of SWE observed in Englehart.

Table 3.5 Backscatter response to SWE in Englehart in 2015.

Date	Site	SWE (mm)	σ° Ku-band (VV, HH, VH)	σ° X-band (VV, HH, VH)
16-Feb-2015	e1	140	-1.60 / -2.28 / -13.77	-2.71 / -5.09 / -14.53
17-Feb-2015	e2	186	-1.79 / -4.31 / -14.39	-4.91 / -6.69 / -15.03
19-Feb-2015	e1	145	-1.44 / -1.23 / -14.37	-3.66 / -5.98 / -13.97
19-Feb-2015	e3	145	-0.79 / -1.28 / -15.01	-3.65 / -5.33 / -13.27

In order to explore the role of depth hoar thickness in the response, it was plotted against SWE and backscatter in three-dimensional plots which are shown in **Figure 3.9**. Observations which were suspected to have been influenced by vegetation or freezing rain have been identified and removed as outliers; these include January 24 and 31 observations at the Hergot site and John's farm, and all observations from March 8, 2015. Backscatter appeared to be a function of both SWE and depth hoar layer thickness, particularly at Ku-band, as backscatter increased along both X- and Y- axes; the largest values of backscatter occur for the largest values of both SWE and depth hoar thickness. For VV and VH polarizations at Ku-band, a cluster of points can be seen with a depth hoar layer thickness of around 45 cm, but with SWE values ranging from the maximum of 186 mm to 145 mm. Despite different SWE values, they demonstrate similar levels of Ku-band VV backscatter of -1.5 dB. In this case it suggests that even as SWE increased to a maximum of 186 mm, the backscatter did not vary for a given depth hoar layer thickness. The three-dimensional plots at X-band showed a weaker influence of SWE and depth hoar layer thickness on backscatter except for the cross-polarized response.

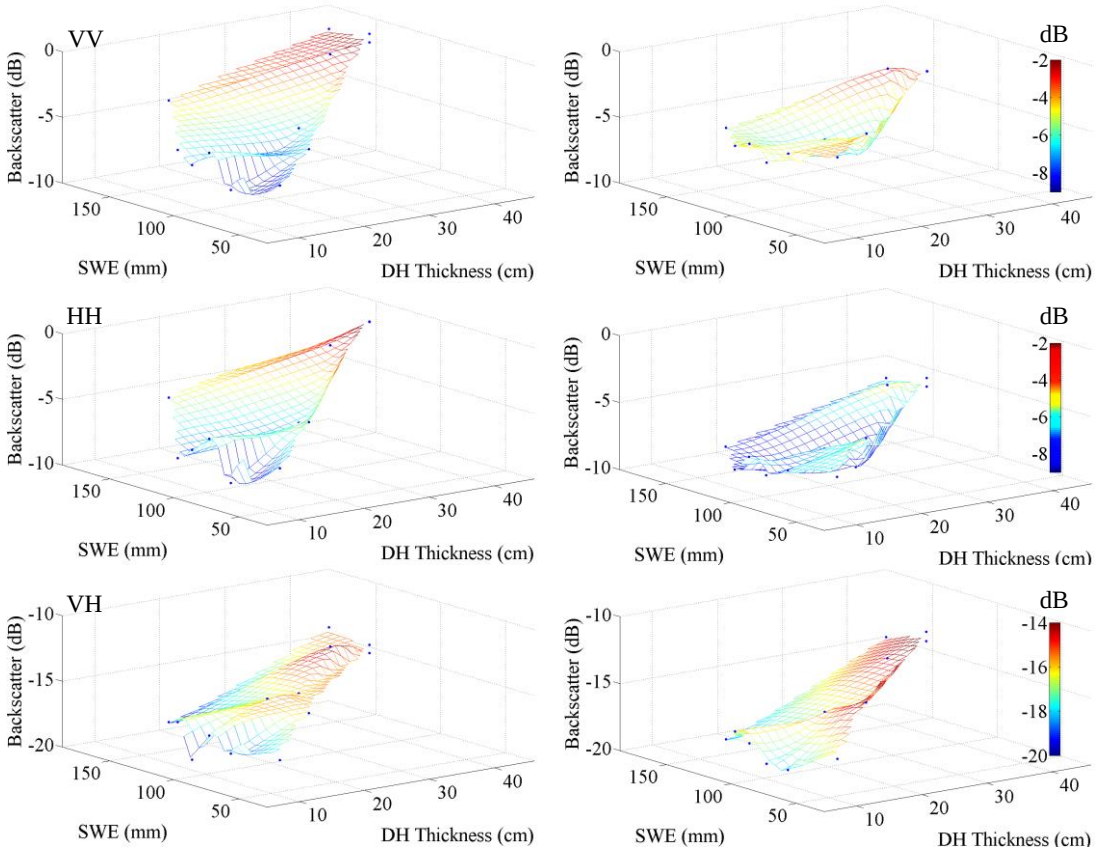

Figure 3.9 Three-dimensional plots of SWE, depth hoar thickness, and backscatter for all sites except suspected outliers. Left-hand column shows Ku-band response and right-hand column shows X-band response.

3.5.3 Polarimetric response

A time series of instantaneous polarization state histograms and polarization signatures for Ku- and X-band at 40° incidence for the Hergot sites are presented in **Figure 3.10** and **Figure 3.11**. This incidence angle was selected for consistency with observations provided in **Figure 3.8** and since it minimizes VV reflectivity within the 34° to 40° incidence range. On December 2, the Ku-band histograms displayed multiple scattered-wave polarization states spanning the range of ellipticity and orientation angles which indicates depolarization. By January 24, and on subsequent dates, the histograms showed a scattered-wave polarization state approximately matching that of the incident wave whereby distinct peaks in the graph were located in the regions associated with vertical and horizontal scattered-wave polarization for vertical and

horizontal incident-wave polarizations respectively; this indicated a reduction in the level of depolarization. Pedestal heights on December 2 were around 0.4 and decreased to around 0.2 or less on Jan 24 and subsequent dates. There was less observable difference between X-band histograms throughout the time series, however the pedestal height decreased from around 0.4 to around 0.2 from December 2 to January 24. Histograms from John's farm site were similar to those of the Hergot site although with a smaller range of scattered-wave polarization states on December 2. Differences in Ku-band pedestal heights between dates at John's farm were less than at the Hergot site, while at X-band they were similar.

At both frequencies, histograms for the Zinger site, all 2013-14 sites, and the Englehart sites indicated consistent like-polarized scattered waves for both vertical and horizontal incident polarizations while pedestal heights of the polarization signatures ranged from 0.1 to 0.3. Thus they appeared similar in shape and distribution to the histograms and polarization signatures shown in **Figure 3.10** and **Figure 3.11** for January 24, 2015 onwards. These figures are provided in Appendix A.

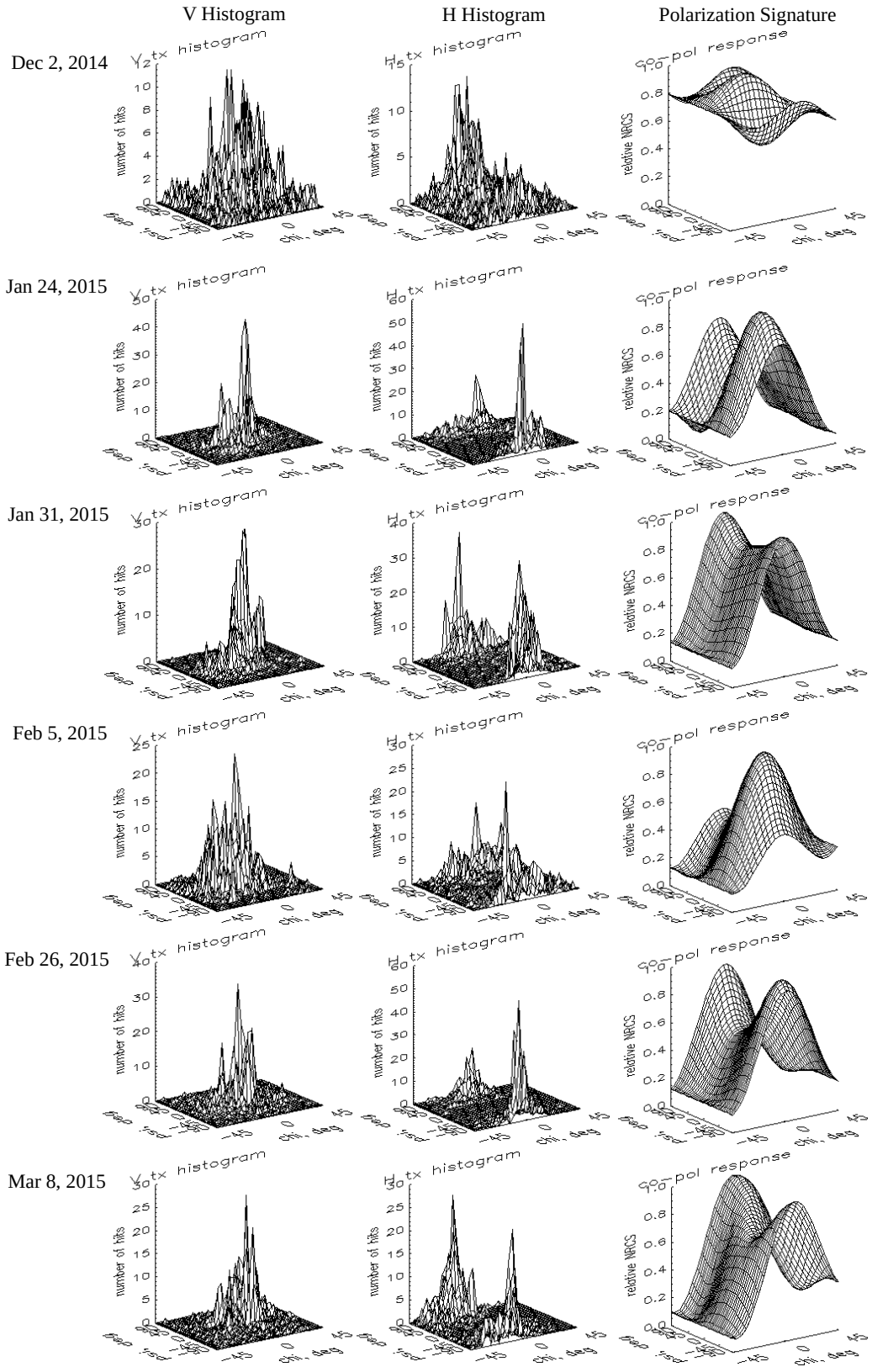

Figure 3.10 Ku-band instantaneous polarization-state histograms and polarization signatures for the Hergot site.

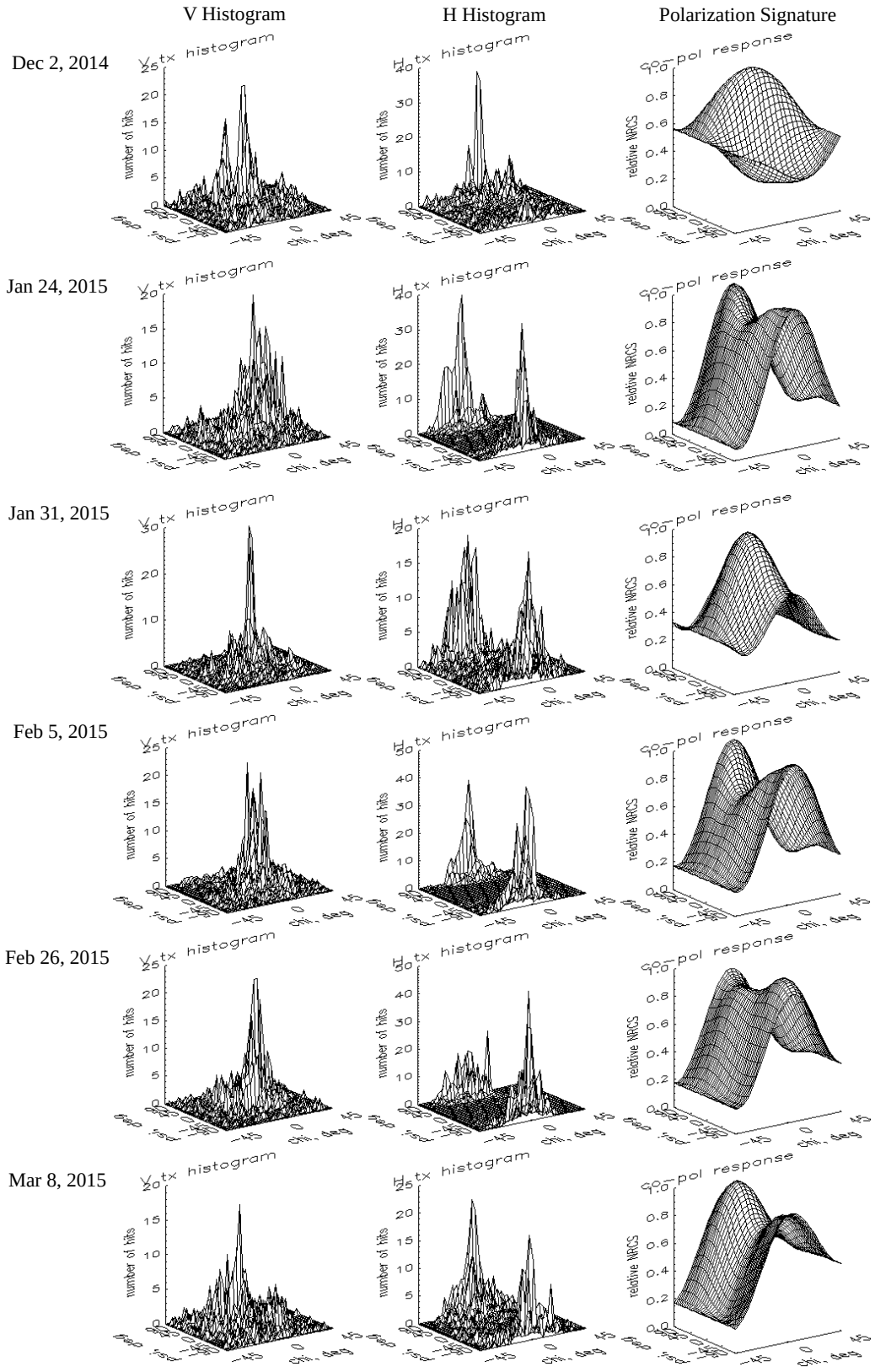

Figure 3.11 X-band instantaneous polarization-state histograms and polarization signatures for the Hergot site.

3.6 Discussion

3.6.1 Combining 2013-14 and 2014-15 observations

A relationship between SWE and Ku-band backscatter was shown in **Figure 3.8** for the 2013-14 Maryhill data in which backscatter increased with SWE. This pattern was consistent across the range of SWE except for an abnormally high level of backscatter for 105 mm of SWE observed at Ku-band on March 21, 2014. Air temperatures above 0°C (**Figure 3.6**) during the day caused surface melt which increased ε' of the snowpack. This enhanced the surface scattering effect, similar to that which was observed by Kendra et al. (1998) in Cadillac, Michigan. A snow density of around 455 kg m^{-3} measured on that day is indicative of melting snow and supports this interpretation (Pomeroy et al., 1998). There was no apparent relationship between X-band backscatter and SWE. The magnitude of soil scattering was unclear for this data however we expect minimal directional influence since the RMS values were similar in both directions.

There were no clear patterns in the 2014-15 Maryhill data. The initial snow-free measurements at the 2014-15 Maryhill sites occurred on December 2. At that time the soil was fluctuating around 0°C at the Zinger site, and was non-frozen at the Hergot site so it contained liquid water which caused an elevated backscatter response. The low stand vegetation, especially at the Hergot site, likely also contributed to the increase in Ku backscatter for both the co- and cross-polarized response; VH backscatter was around -14 dB at the Hergot site compared to about -16 dB for the Zinger site and John's farm site on December 2.

The spread of the histograms and the elevated pedestal in **Figure 3.10** indicated that substantial Ku-band wave depolarization was occurring at the Hergot site and John's farm, but not at the Zinger site, on December 2. **Figure 3.11** shows less evidence of depolarization at X-

band in comparison to K-band since the histograms displayed a smaller relative spread of polarizations and the pedestal, while greater than subsequent dates, was less than the Ku-band pedestal by about 0.2 units. On this date, there was no snow and the vegetation in the field at the Hergot site and John's farm consisted of new growth and coarse stalks from an earlier harvest. The new growth was dense and randomly oriented, masking the row orientation in the field and acting as a depolarizing scatterer, marked by an elevated pedestal height and a range of ellipticity and orientation angles in the instantaneous polarization-state histograms. McNairn et al. (2002) reported similar indication of depolarization for crop residue and senesced crops at C- and L-band frequencies. By January 24, nearly 15 cm of snow had fallen and the amount of depolarization was less than on December 2. The plots in **Figure 3.10** reflect this change with a decrease in the spread of the polarizations in the histograms and a reduced pedestal height in the polarization signature (McNairn et al., 2002). We think the snow had compressed the new growth into a homogenous layer beneath the snow effectively removing the depolarizing scatterer from the scene. The remaining vertical stalks did not depolarize the incident waves. Another possible explanation is that as the season progressed, the live vegetation senesced, and began to dry and freeze as the snow accumulated and air temperatures decreased. Such an occurrence would theoretically mean that the vegetation would become more transparent to the microwaves (McNairn et al. 2001). A similar explanation was suggested by Yueh et al. (2009) who observed a decrease in the radar response, at Ku-band, of coniferous trees throughout a winter observation period. However, McNairn et al. (2001) found that senesced corn and barley residue still contained water in the fall and influenced radar backscatter, but freezing would likely reduce this influence through a reduction in ε' as liquid water within the vegetation froze. Because no measurements of the vegetation condition such as water content, or ε', were made,

we cannot say with certainty what caused this effect. Similar levels of depolarization were not observed at the Zinger site, Engelhart sites, or in the 2013-14 data because these sites were not vegetated. From these observations it is suggested that vegetation can play a strong role as a depolarizing scatterer within the early season snowpack at these frequencies. Further investigation of this feature is needed to fully understand this issue.

Although the scattered-wave depolarization had decreased after December 2 at the Hergot site and John's farm, the backscatter still remained notably high on January 24 and January 31. While the snowfall prior to the January 24 observation may have compressed the new growth, the coarse older stalks remained standing. Furthermore, micro-wells had developed around each stalk which left much of the stalks exposed despite the 15 cm of accumulated snow. These exposed stalks caused the elevated backscatter response seen on January 24. By January 31 additional snow had accumulated, burying more of the stalks and filling in the micro-wells which corresponded with a decrease in backscatter. By February 5, the vegetation was completely covered by snow and the backscatter decreased again. However the vegetation was just barely covered and so likely influenced backscatter from within the snowpack. **Figure 3.12** shows the progression of accumulation and the associated Ku-band backscatter over this time period.

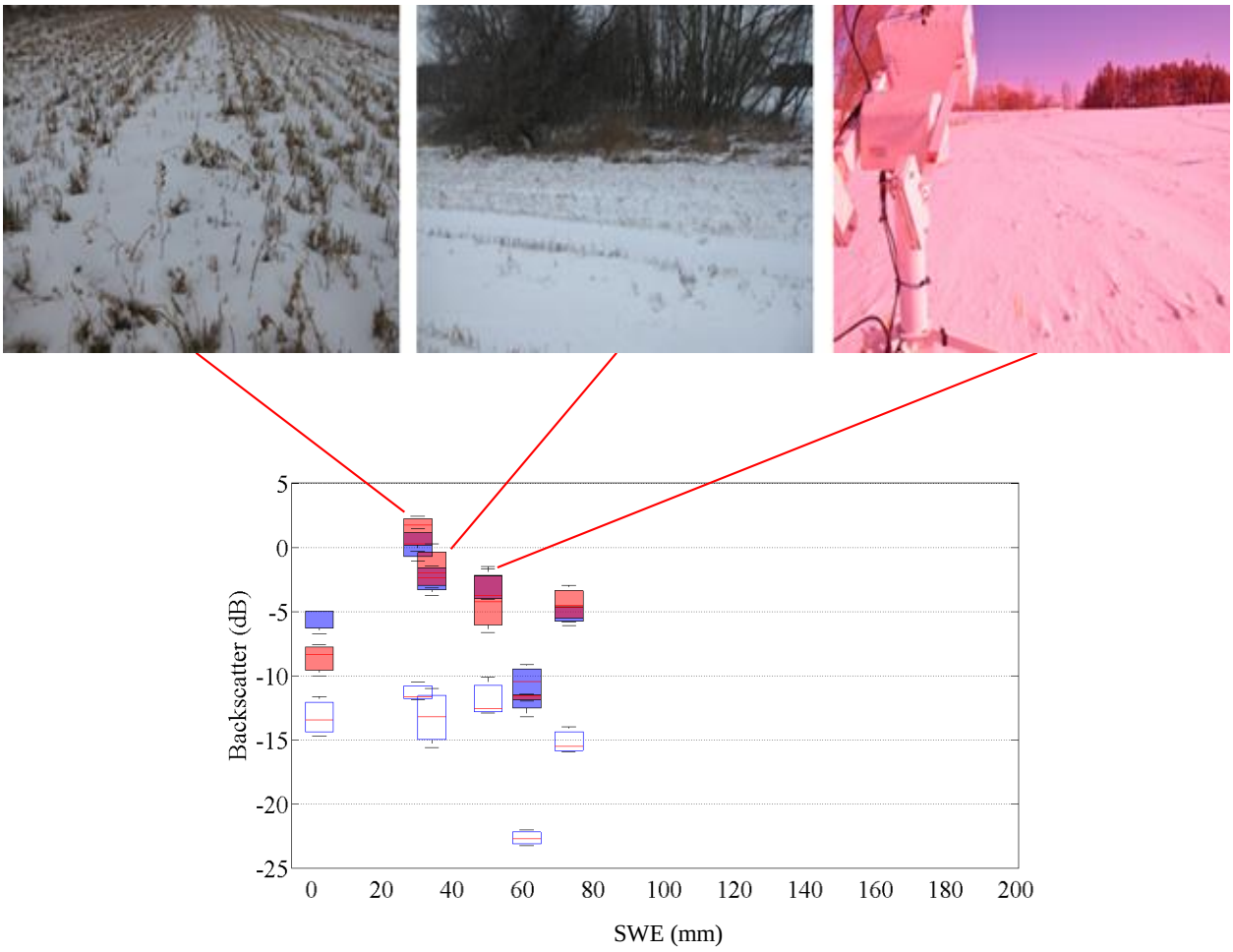

Figure 3.12 Progression of snow accumulation at the Hergot site on January 24 (top left), January 31 (top centre), and February 5 (top right), compared with Ku-band backscatter.

Observations on March 8, 2015 produced low backscatter at all Maryhill sites. Preceding the March 8, 2015 observation a freezing rain event occurred which deposited a 5 mm ice layer on top of the snowpack. The dielectric contrast between air and ice created a surface scattering effect at the air-ice interface. However, we suspect the smooth ice surface combined with the off-nadir incidence angles enhanced forward scattering of the waves leading to a reduction in backscatter observed at both frequencies as shown in **Figure 3.8** at 125, 59, and 141 mm SWE for the Zinger site, Hergot site, and John's farm, respectively.

The elevated RMS soil roughness at the Hergot site was caused by a regular series of directional troughs and furrows. Surface roughness was thereby enhanced in the direction perpendicular to the crop rows which can impact co-polarized radar backscatter (McNairn et al., 2001). The scatterometer was positioned such that the look direction was parallel to these rows so that scanning would be done across the rows and the impacts of this roughness would be averaged in each scan line and common to each incidence angle. Therefore the effect on the data of the directional nature of the crop rows was minimized. A strong directional nature in the soil features was not present at other sites, which is common in such crops since they are generally not cultivated annually and allowed to grow for several years, resulting in relatively smooth surface characteristics (Ulaby et al., 1975).

When all of the data points, excluding those influenced by vegetation, freezing rain, or non-frozen soil as discussed above, were plotted on the same backscatter-SWE curve as illustrated in **Figure 3.13**, a relationship between backscatter and SWE at Ku-band was evident; such relationship was not apparent at X-band. Furthermore results from the 2014-15 season replicated and confirmed results from the 2013-14 season.

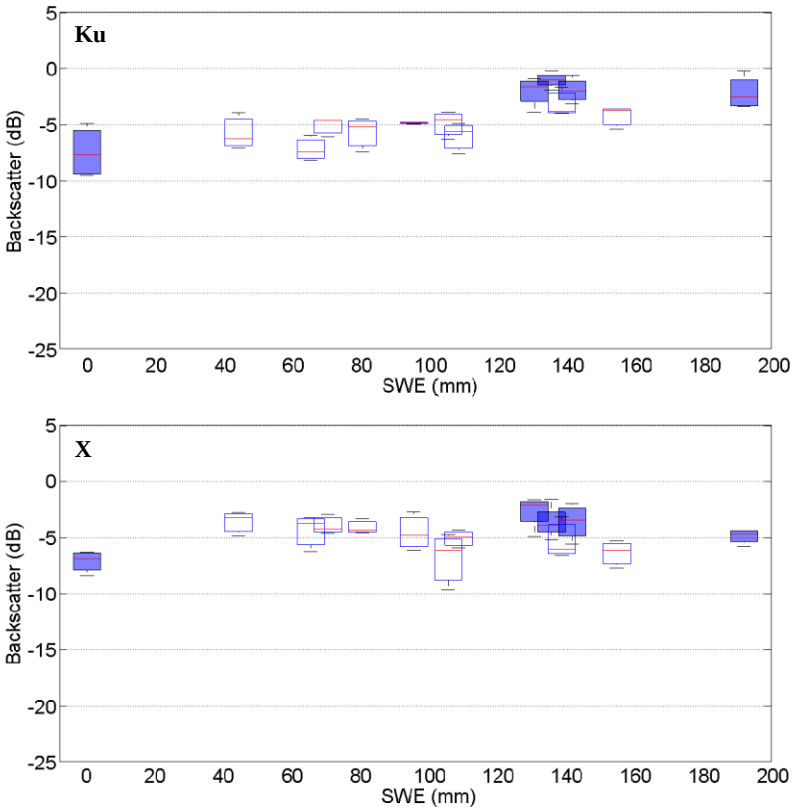

Figure 3.13 Multiple observations plotted together. Maryhill data are represented by transparent boxes while Englehart data are coloured blue. Only VV polarization is shown for clarity.

Figure 3.13 also highlights sensitivity of Ku-band signals to SWE from 0 to 140 mm. Beyond this level of SWE, backscatter no longer increased, but stayed relatively constant around -3 dB indicating a loss of sensitivity. This suggested that Ku-band observations can only detect snow accumulation up to about 140 mm of SWE. **Figure 3.9** replicates this result in terms of the backscatter response to SWE, but while SWE increases beyond 140 mm, depth hoar thickness stays relatively constant. This suggests that the backscatter was responding more strongly to depth hoar in the snowpack than to SWE. Had the depth hoar layer continued to grow in terms of both grain size and layer thickness, backscatter likely would have continued to increase. Such an outcome is largely theoretical however since an overall increase in snow depth would decrease the thermal gradient required for depth hoar formation and growth. Conditions for

depth hoar development are typically more favorable in low-accumulation snowpacks which are exposed to a stronger temperature gradient than a thicker snowpack in the presence of the same air and basal temperatures, and therefore can lead to more depth hoar development than in a thicker snowpack which will be exposed to a weaker temperature gradient under the same conditions (Sturm & Benson, 1997). Revisiting **Figure 3.7** we see that the depth hoar layer thickness grew throughout the season at the Hergot site and John's farm, but stayed relatively constant at the Zinger site. Accounting for the effects of vegetation and freezing rain at the Hergot site and John's farm, the backscatter may have been responding to the developing depth hoar layer. Similarly the relatively flat relationship in **Figure 3.8** for the Zinger site may have corresponded with a depth hoar layer that remained at a relatively constant thickness.

Under the suggestion that depth hoar was driving the radar response, the observations from all sites were reordered by density-weighted grain size (DWGS) instead of by SWE, as shown in **Figure 3.14**. DWGS was used because it allows us to account for the mass of scatterers per known volume in the layer and not just the layer thickness thus conserving mass and providing a truer indication of each layer's scattering properties. In order to calculate the DWGS, a weighting for each individual layer was determined from the ratio of layer density to the sum of densities for all layers and was then applied to the grain size of each corresponding layer. The density-weighted grain size for each layer was then summed to provide a DWGS representative of the entire snowpack. See Appendix B for a sample calculation of DWGS.

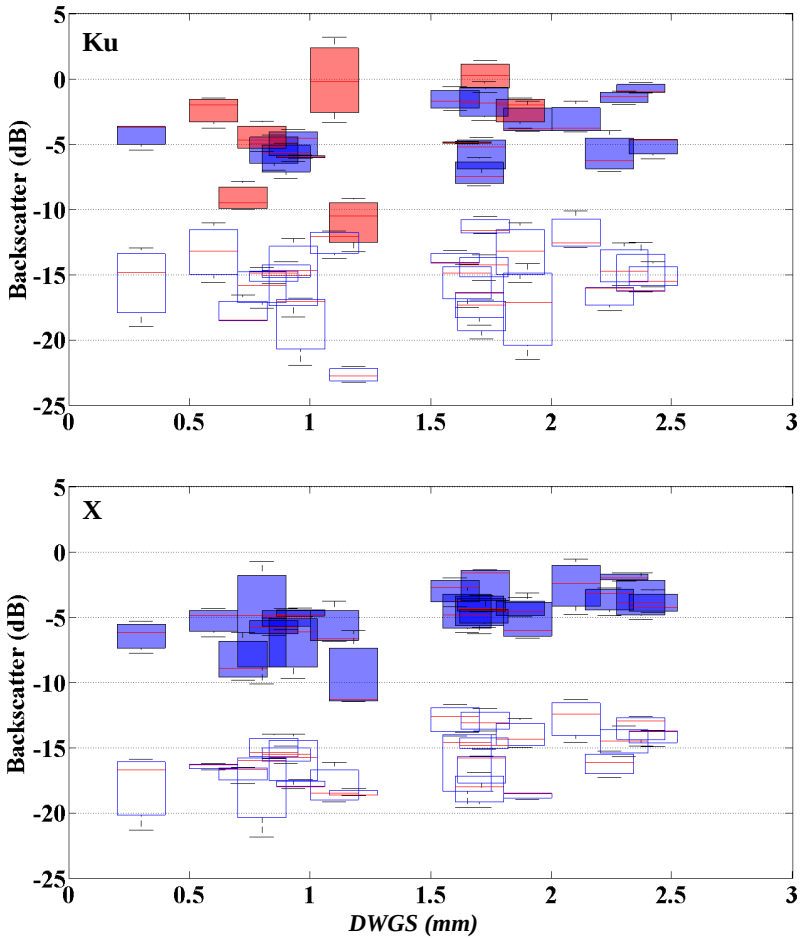

Figure 3.14 Observations ordered by DWGS. Blue rectangles represent VV polarization and white rectangles represent VH polarization. HH polarization was omitted for clarity but was similar to VV polarization. Outliers remain in the dataset and are coloured red in the Ku-band plot.

The relationship between DWGS and backscatter at Ku-band appears ambiguous. The influence of vegetation, non-frozen soil, and ice rain is still present in the co- and cross-polarized response. At X-band however, the influence of vegetation, non-frozen soil, and ice rain appears much less prevalent and there is an apparent relationship between grain size and backscatter in both the co- and cross-polarized response. Backscatter appeared to consistently increase with grain size and did not level off at any point as it did in the SWE plots. This indicates sensitivity across the entire range of grain size. Taken together with the surface plots in **Figure 3.9**, this strengthens the argument that grain size has a stronger influence on backscatter than SWE.

3.6.2 Using MEMLS3-A to investigate the influence of grain size

To investigate the influence of grain size on backscatter, the Microwave Emission Model of Layered Snowpacks model, version 3, adapted for active microwave backscatter (MEMLS3-A), was used. MEMLS-3A is an electromagnetic model that uses a six-flux theory to describe radiative transfer through an n-layer snowpack in the frequency range of 5 – 100 GHz (Wiesmann & Mätzler, 1999). The model, originally developed for passive microwave applications, uses Kirchoff's law to derive reflectivity (r) from emissivity (e) where $r = 1 - e$ (Proksch et al., 2015b). Input parameters explicitly characterize each layer in terms of layer thickness, temperature, volume fraction of liquid water, density, salinity, and exponential correlation length (p_{ex}). However field observations in this study used D_{max} to estimate grain size so a conversion was required. Durand et al. (2008) found a linear relationship between p_{ex} and the natural logarithm of D_{max} for volume fractions (v) > 0.2, where v is defined as the ratio of the densities of snow and ice. For $v \leq 0.2$, p_{ex} is 0.05 mm and was determined by averaging p_{ex} values in a test dataset for observations where $v \leq 0.2$. The relationship follows, where a_0 and a_1 are best-fit parameters valued at 0.18 and 0.09:

$$p_{ex} \begin{cases} a_0 + a_1 \, ln \, D_{max} \pm 0.03 \, mm, & v > 0.2 \; and \; D_{max} > 0.125 \, mm \\ 0.05 \pm 0.015 \, mm, & otherwise \end{cases} \tag{3.2}$$

Three special cases were investigated using MEMLS3-A with a simplified snowpack: the first two cases (case 1 and case 2) used a two-layer snowpack consisting of a large-grained layer, representing depth hoar, and a small-grained layer while the third case used a single layer snowpack. Operational parameters were matched to those of the study. Snowpack parameterization for these tests is provided in **Table 3.6**. Layer temperature, density and grain size (D_{max}) were matched to common values observed in Englehart. The large-grain size

represented by D_{max} of 3.5 mm in cases 1 and 2 was a commonly observed value of D_{max} for depth hoar. The small-grain size represented by D_{max} of 0.5 mm was chosen to represent a clear distinction from the large-grained layer, and was also commonly observed in non-depth hoar layers in Englehart. The conversion from D_{max} to p_{ex} was completed using the method of Durand et al. (2008). In case 1, the snowpack depth was held constant along with all other parameters except for the thickness of the large-grained layer, which was allowed to increase iteratively at the expense of the small-grained layer. This test mimicked the development of depth hoar within a snowpack of a fixed depth and was designed to test the radar response to a growing depth hoar layer. In case 2, the thickness of the large-grained layer was held constant along with all other parameters except for the thickness of the small-grained layer which was allowed to grow iteratively, effectively increasing the overall depth of the snowpack. This test mimicked an increase in depth of the snowpack while the depth hoar layer remained at a constant thickness and was designed to test the radar response to an increase in SWE with no change in the depth hoar layer. In case 3 the grain size of a single layer snowpack was iteratively increased from a D_{max} of 1 to 4 mm in four steps. This test investigated the radar response to increasing grain size only.

Table 3.6 MEMLS3-A parametrization for three cases. Volumetric fraction of liquid water and salinity were held at 0. D_{max} was converted to p_{ex} using the method by Durand et al. (2008) for implementation in the model. Layer number 1 represents the lower layer in the snowpack and layer number 2, where present, represents the upper layer. Depth hoar is abbreviated to DH.

Case	Step	Layer Number	Temperature (K)	Liquid Water (%)	Density (kg m^{-3})	Layer Thickness (cm)	Salinity (ppm)	p_{ex} (mm)	D_{max} (mm)
1	1	1	270	0	230	1	0	0.29	3.5
		2	250	0	300	59	0	0.11	0.5
	2	1	270	0	230	15	0	0.29	3.5
		2	250	0	300	45	0	0.11	0.5
	3	1	270	0	230	30	0	0.29	3.5
		2	250	0	300	30	0	0.11	0.5
	4	1	270	0	230	45	0	0.29	3.5
		2	250	0	300	15	0	0.11	0.5
	5	1	270	0	230	59	0	0.29	3.5
		2	250	0	300	1	0	0.11	0.5
2	1	1	270	0	230	15	0	0.29	3.5
		2	250	0	300	1	0	0.11	0.5
	2	1	270	0	230	15	0	0.29	3.5
		2	250	0	300	15	0	0.11	0.5
	3	1	270	0	230	15	0	0.29	3.5
		2	250	0	300	30	0	0.11	0.5
	4	1	270	0	230	15	0	0.29	3.5
		2	250	0	300	45	0	0.11	0.5
	5	1	270	0	230	15	0	0.29	3.5
		2	250	0	300	60	0	0.11	0.5
3	1	1	260	0	230	50	0	0.18	1.0
	2	1	260	0	230	50	0	0.24	2.0
	3	1	260	0	230	50	0	0.28	3.0
	4	1	260	0	230	50	0	0.31	4.0

MEMLS3-A predictions for case 1 and case 2 are shown in **Figure 3.15**. A noticeable increase in backscatter occurred across all incidence angles at both frequencies, with the first increase in depth hoar layer thickness. Ku-band backscatter increased by nearly 5 dB while X-band backscatter increased by nearly 4 dB. For subsequent increases in thickness, backscatter continued to rise but the difference was smaller with 2 dB or less separating each subsequent increase in thickness. The pattern remained consistent across all incidence angles. In case 2 there was virtually no difference in backscatter at either frequency as SWE increased.

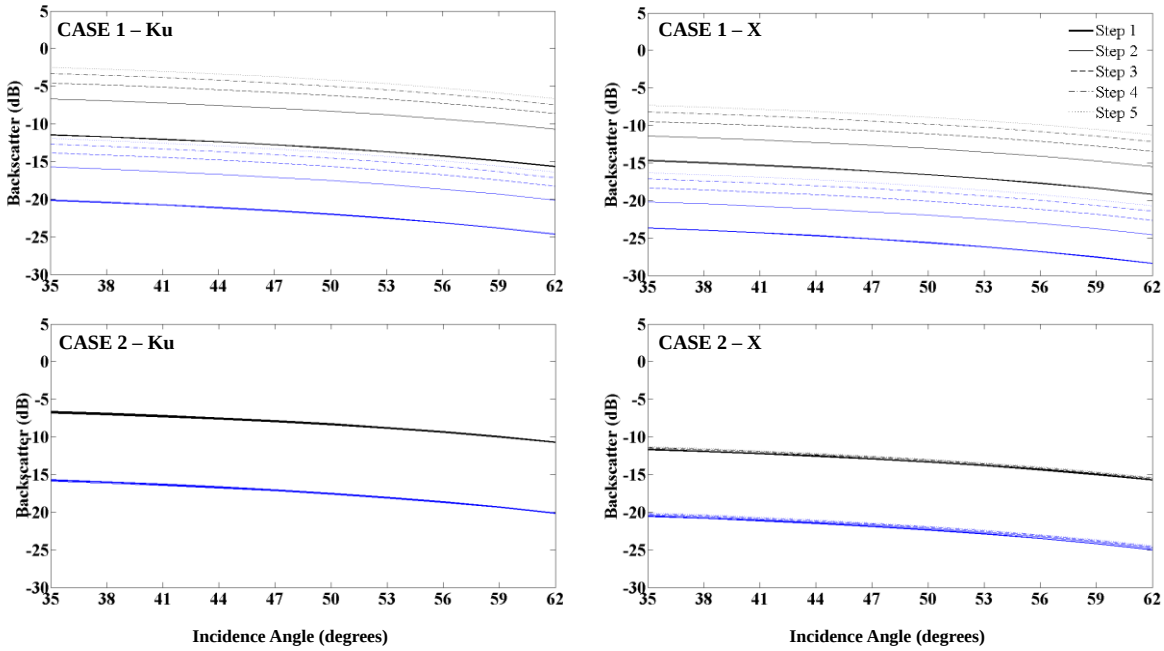

Figure 3.15 MEMLS3-A backscatter predictions for case 1 and case 2. VV (black line) and VH (blue line) polarizations have been shown for Ku- and X-band frequencies. HH polarization has been omitted for clarity but was similar to VV polarization.

MEMLS3-A predictions for case 3 are shown in **Figure 3.16**. The pattern is similar to that of case 1 for both frequencies. With the first increase in grain size there was a 3 dB increase in backscatter at both frequencies. Subsequent increases in grain size resulted in increasingly smaller increases in backscatter ranging from less than 2 dB to nearly 1 dB. This was consistent across all incidence angles.

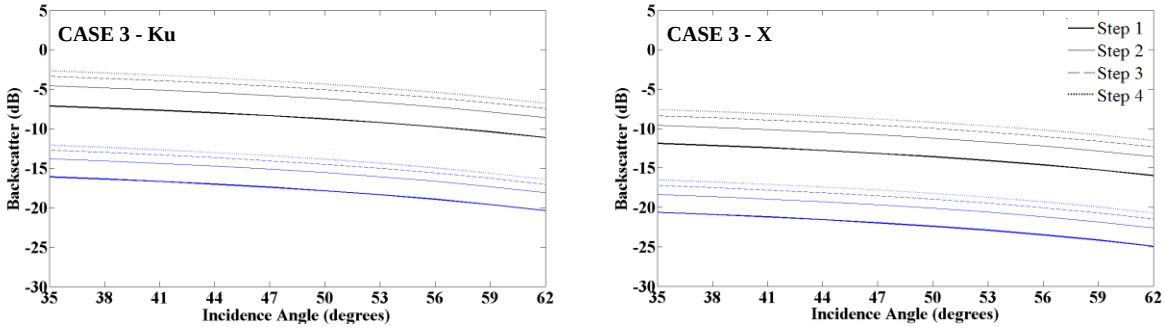

Figure 3.16 MEMLS3-A prediction for case 3. Grain size of a single layer pack was incremented in four 1 mm steps. Black line represents VV polarization while blue line represents VH.

The combined results of the three special cases support the argument that the backscatter response was more heavily influenced by grain size than by SWE alone. From the model observations, the influence of large-grained layer thickness appeared to be slightly stronger than that of grain size alone, when all other variables were held constant. This points to the importance of the relative number of scatterers interacting with the waves since the number of scatterers would increase with an increase in layer thickness, however as grain sizes continue to grow, approaching λ, Mie scattering could produce a stronger effect on backscatter. While these results highlight the relative importance of grain size compared with SWE in terms of radar response, they do not suggest the mechanism behind their influence. As a point of clarification, note that MEMLS3-A was parameterized based on grain size only and not by grain type so it says nothing about the effects of grain type or shape. In other words we cannot say whether depth hoar itself has caused these model predictions, but rather spherical snow grains of a particular size. This poses the question of what microstructural aspect is actually causing this response: is it strictly grain size or does the shape, and number of scatterers, have an influence as well?

3.6.3 Sources of error

The results of case 1, 2 and 3 in **Figure 3.15** and **Figure 3.16** underscore the relative importance of grain size in terms of active microwave remote sensing, and therefore highlight a critical limitation of this study. In the field a gridded comparator card and hand lens were used to observe D_{max} as a proxy for grain size. Results from this subjective method vary with the observer and can be inaccurate (Painter et al., 2007). There was also error associated with the conversion from D_{max} to p_{ex} as seen in **Figure 3.17**. If we consider only that error, specified in (3.2), MEMLS3-A predicts a difference of nearly 3 dB at Ku-band for the co-polarized vertical

response and over 2.5 dB for the cross-polarized response for a D_{max} of 1 mm; magnitudes are slightly less at X-band. The error introduced by the conversion is likely larger than that introduced by in-field D_{max} measurements and thus underscores the need for a better relationship between D_{max} and p_{ex} or a more accurate field method for estimating grain size (Durand et al., 2008).

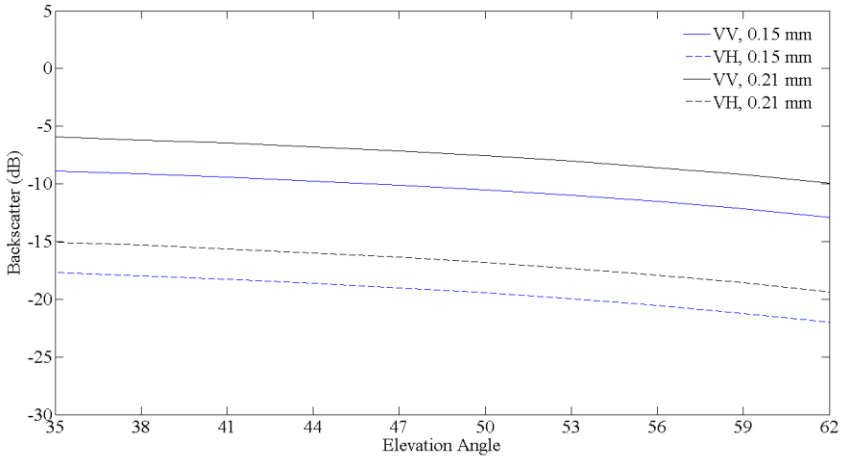

Figure 3.17 Effects of grain size error introduced by conversion from D_{max} to p_{ex}.

Uncertainty in grain size estimation was also introduced with the assumption that grain characteristics observed at one snow pit adjacent to the field of view were representative of the entire scene since large spatial variability can exist on the scale of metres (Marshall et al., 2007; Sturm et al., 2004). Our sites were generally in exposed areas, devoid of drifts and other visible small-scale features; for this reason, we suspect the snowpack characteristics in the field of view were relatively homogeneous therefore minimizing the impacts of spatial heterogeneity. A more rigorous approach would employ trench-style snow pit observations as in Tape et al. (2010).

Snowpack characterization provided another source of error in terms of identifying the position of distinct snow layers, especially those consisting of depth hoar. There was often no

clear delineation between layers. Instead, they were often separated by a gradient of grain types and sizes and so determining layer position required a subjective judgement from the observer. This becomes especially important when parameterizing a model such as MEMLS3A with snowpit observations. Given the likelihood of error introduced at this step, parameterizing a model with snowpit observations could result in substantial error.

In terms of overall error of the study, we need to include the error introduced by the UW-SCAT measurements and post-processing procedures. The combined systematic and random post-processing error associated with UW-SCAT was estimated at ± 2.0 dB (King et al., 2015). Uncertainty introduced during the scatterometer observations was generally caused by human error which included improper levelling of the equipment, inaccurate sighting of the in-scene calibration target, and inaccurate measurement of sensor height and distance to the calibration target. Another source of error in the study involved the accuracy of equipment positioning throughout the season. Efforts were made, using markers at the sites and GPS receivers, to ensure accurate positioning of the equipment throughout however there was likely some lateral shift in platform position in time; positional error was estimated at about ± 5 cm in each lateral direction. Because of the signal averaging in the azimuth direction, this error likely had a minimal impact on observations. Despite these sources of error and uncertainty, the results from this study appear reasonable when compared to output from MEMLS3-A and previous studies; they also proved to be repeatable over the two years of observations.

3.7 Conclusion

A range of SWE from 0 to 186 mm was observed using a ground-based polarimetric scatterometer at Ku- and X-band frequencies over two winters and 26 observations in Maryhill and Englehart, Ontario. Results from the 2014-15 season replicated and confirmed results from

the 2013-14 season. From these observations it appeared that that Ku-band backscatter increased with SWE up to 140 mm after which point reduced sensitivity was observed, while X-band did not respond to these levels of SWE. However, an investigation of the seasonal depth hoar evolution suggested that the backscatter was responding to development of the depth hoar layers instead of SWE and that once growth of those layers ceased, backscatter no longer increased. MEMLS3-A, an electromagnetic model, was used to test the radar response to increasing grain size within a simplified snowpack. Results of this test showed that these frequencies were more strongly influenced by an increase in grain size than an increase in SWE. Through evaluation of the polarimetric response in these conditions vegetation was found to play a strong role as a depolarizing scatterer within the early season snowpack; increased snow accumulation decreased depolarization to levels common with non-vegetated sites.

MEMLS3-A also highlighted a major source of uncertainty in this study. Grain size was shown to exert considerable control on the radar response and it follows that accurate estimation of this parameter in the field is paramount. Field estimates of grain size were subjective and likely introduced considerable variance from the true value.

Overall, these results suggest that the Ku- and X-band frequency respond as strongly, if not more so to the presence and development of depth hoar within the snowpack than to accumulation of SWE. With this in mind future work should be directed at exploring the nature of the relationship between depth hoar and backscatter at these frequencies with respect to the relative magnitude of the effects of grain size and shape: is the elevated backscatter more strongly influenced by the increase in grain size, the faceted shape of depth hoar crystals, or some combination thereof?

Chapter 4 Thesis conclusions

This thesis explored the response of Ku- and X-band microwaves to a series of seasonal, mid-latitude snowpacks in agricultural fields in Maryhill, and Englehart Ontario during the winters of 2013-14 and 2014-15. In order to quantify and characterize the microwave response, 26 observations were made over a range of snow depths up to 67 cm, corresponding to 186 mm of SWE. As in earlier studies, an apparent relationship between Ku-band backscatter and SWE was observed but sensitivity was reduced beyond 140 mm of SWE, with no appreciable increase in backscatter up to the maximum observed value. The loss of sensitivity contrasted with the theory that supported penetration in these conditions beyond the observed snow depths. It is suggested, therefore, that other mechanisms were driving the response. A comparison of the seasonal evolution of depth hoar with backscatter revealed an apparent relationship between the DWGS of a snowpack and backscatter at both frequencies. However, while this relationship was more apparent at X-band, the effects of underlying vegetation, ice layers, and non-frozen ground in the early season tended to mask this relationship at Ku-band. MEMLS3-A was used to simulate the development of depth hoar and non-depth hoar layers in three simple scenarios designed to investigate the radar response to grain size. Backscatter was shown to increase, at both frequencies, when the thickness of the depth hoar layer was increased, at the expense of the non-depth hoar layer, and also when the grain size of a single-layer snowpack was iteratively increased. Backscatter did not substantially increase when only the thickness of the non-depth hoar layer was increased. Overall these simulations supported the hypothesis that grain size had more influence over the backscatter response than SWE, but it was not clear whether it was the grain size, the thickness of the depth hoar layers, or the grain shape (unaccounted for in the model) that was driving this effect.

The polarimetric response of the snowpack in this environment was investigated and found to yield important information that was not apparent from backscatter alone. The use of polarimetric data was shown to be a useful tool for understanding microwave interactions with a target especially in terms of depolarization. Using polarimetric data, the early season response of dense, low lying subnivean vegetation was identified in the winter of 2014-15. Early season depolarization along with elevated backscatter was observed in the presence of dense vegetation in and beneath the snowpack, especially at Ku-band. As snow accumulated, much of the vegetation was matted down and its influence on depolarization and backscatter was tempered. The backscatter and amount of depolarization subsequently returned to levels common to other non-vegetated sites observed in the study. Further use of the polarization histograms and signatures could include investigation of wave interaction with changing snow microstructure and stratigraphy. Furthermore, the shape of the polarization signatures could provide information on wave interaction but was not exploited in this thesis.

Sources of uncertainty in this study stemmed largely from human error, specifically in the estimation of grain size in the field. Methods such as the use of SMP combined with multiple grain size estimations in snow pits could have improved the accuracy of the estimations. Other sources of human error likely resulted from measurements of system height and distance to the in-scene calibration target. Although positional inaccuracy of the scatterometer with each site visit contributed to the overall error, these impacts were minimized by averaging across each azimuth scan. Error associated with post-processing of the radar data was estimated at ± 2.0 dB. Despite these sources of error, the results appeared appropriate when compared to other studies, and were repeatable from one year to the next.

The results of this thesis give direction to future studies on the interaction of snow and Ku- and X-band radar. The effects of grain size and shape on the radar return need to be better understood and separated from each other. Research should continue to focus on these microstructural aspects and their inter-relationships to determine whether the increase in observed backscatter was caused simply by an increase in grain size or if snow layer morphology and orientation of depth hoar grains in the snowpack exerts a significant controlling influence. The field data set collected in this thesis, in conjunction with electromagnetic models such as MEMLS3-A, can provide a starting point to do so.

APPENDIX

Appendix A

A Polarization histograms and signatures

Instantaneous polarization-state histograms and polarization signatures at Ku- and X-band frequencies for all sites and dates are provided in the following figures. A detailed explanation of figure interpretation is provided in section 3.4.4.

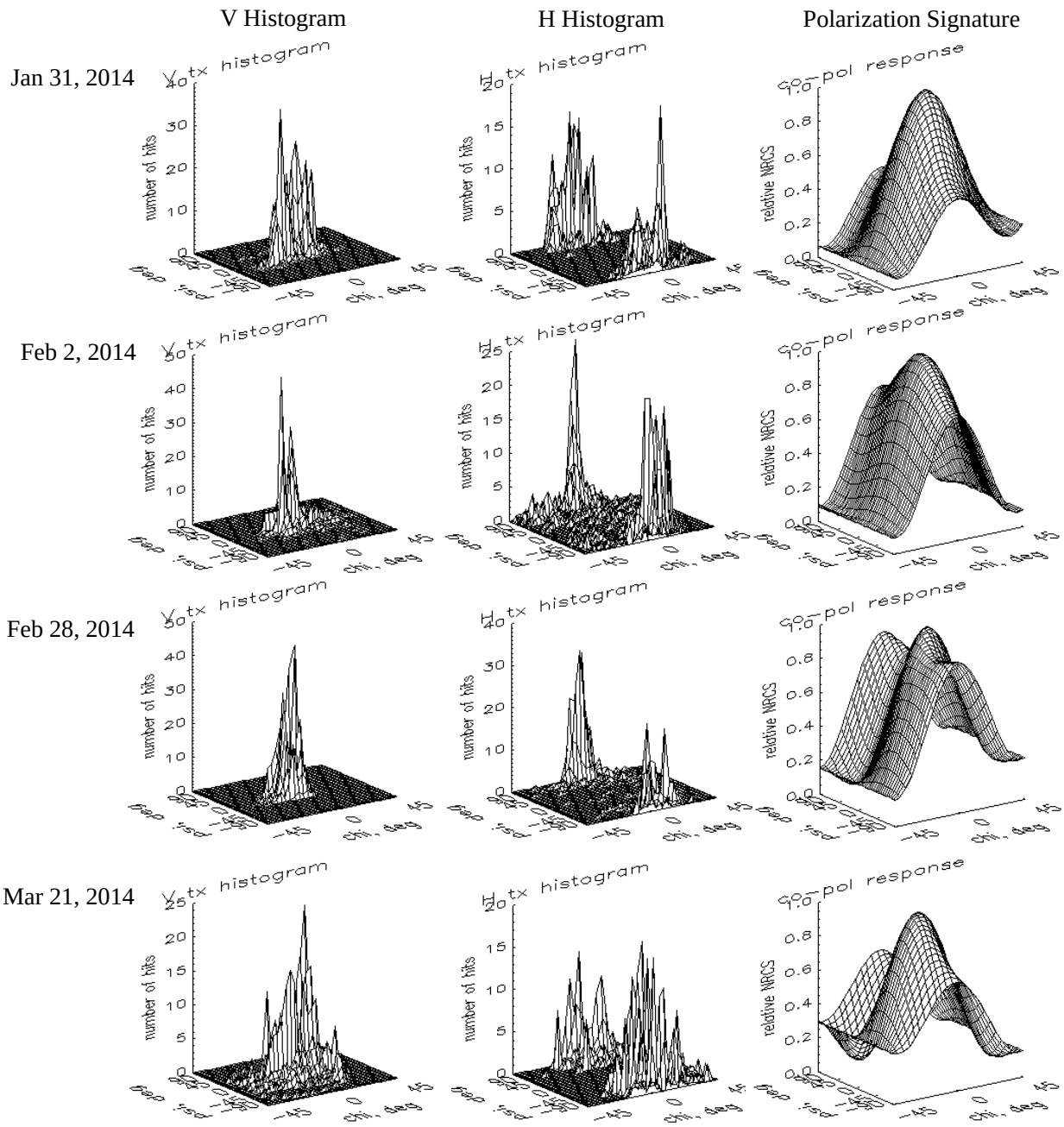

Figure A 1 Polarization histograms and signatures for Ku-band, 2013-14 season.

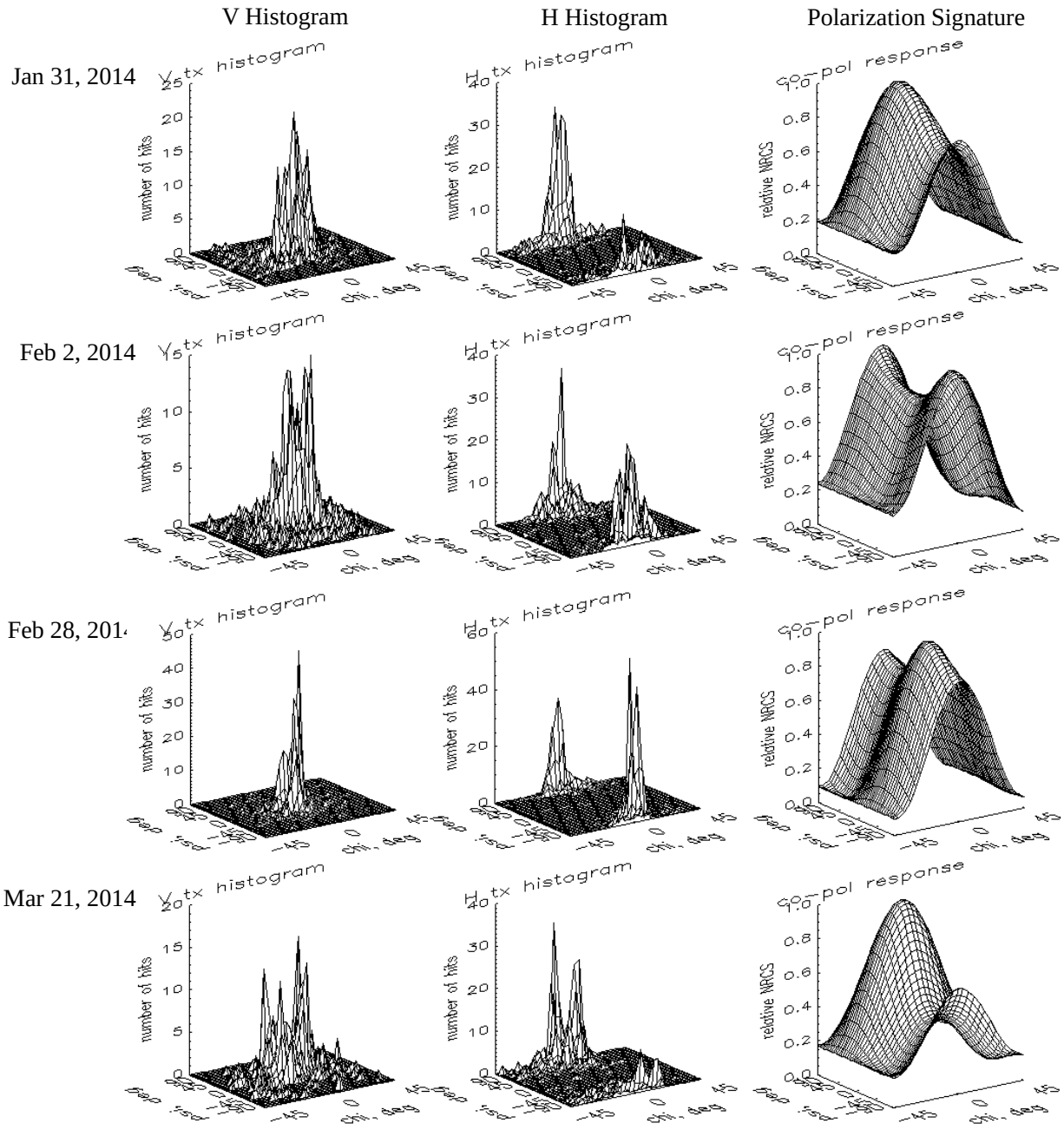

Figure A 2 Polarization histograms and signatures for X-band, 2013-14 season.

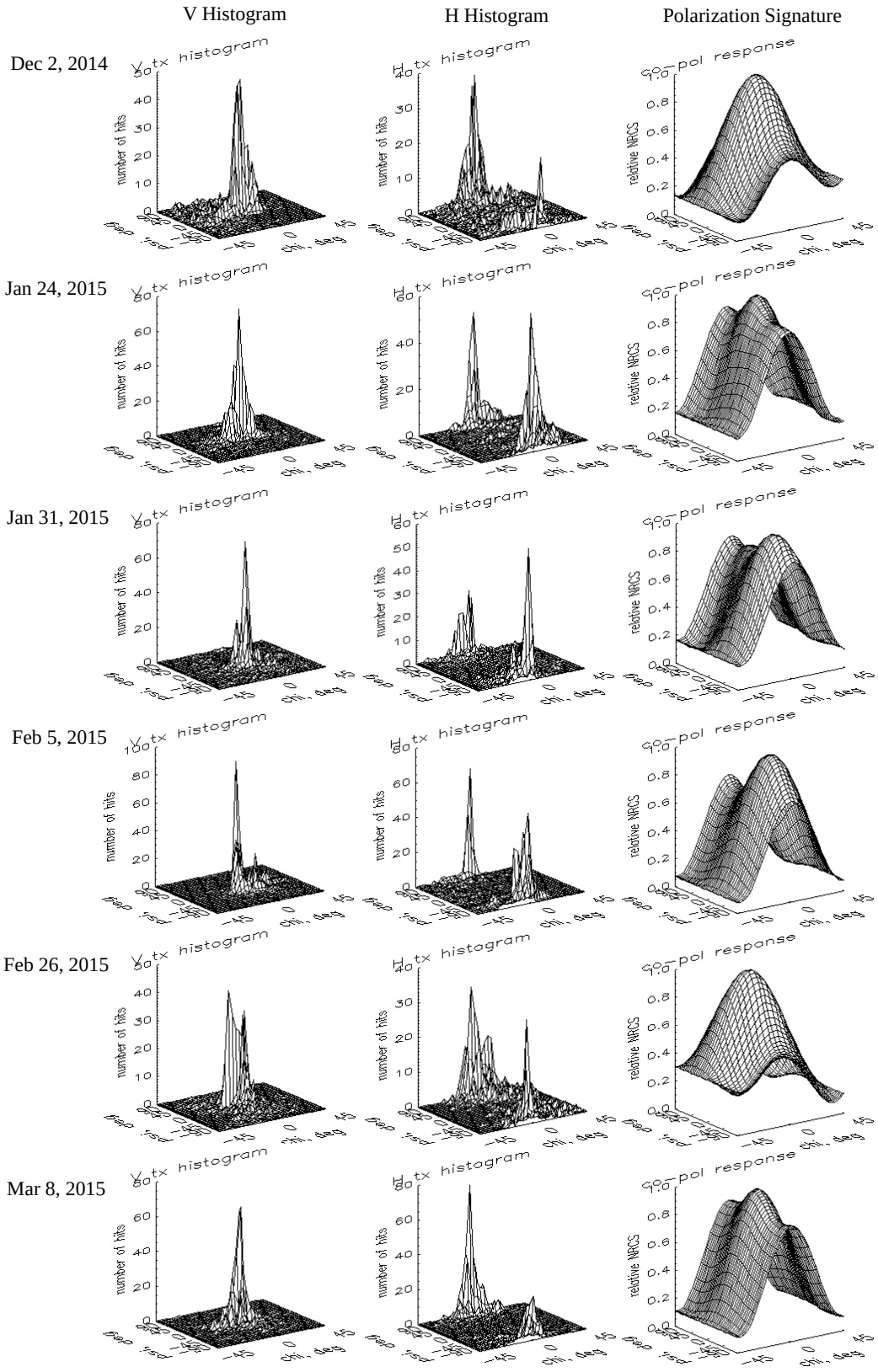

Figure A 3 Polarization histograms and signatures for Ku-band, 2014-15 season, Zinger site.

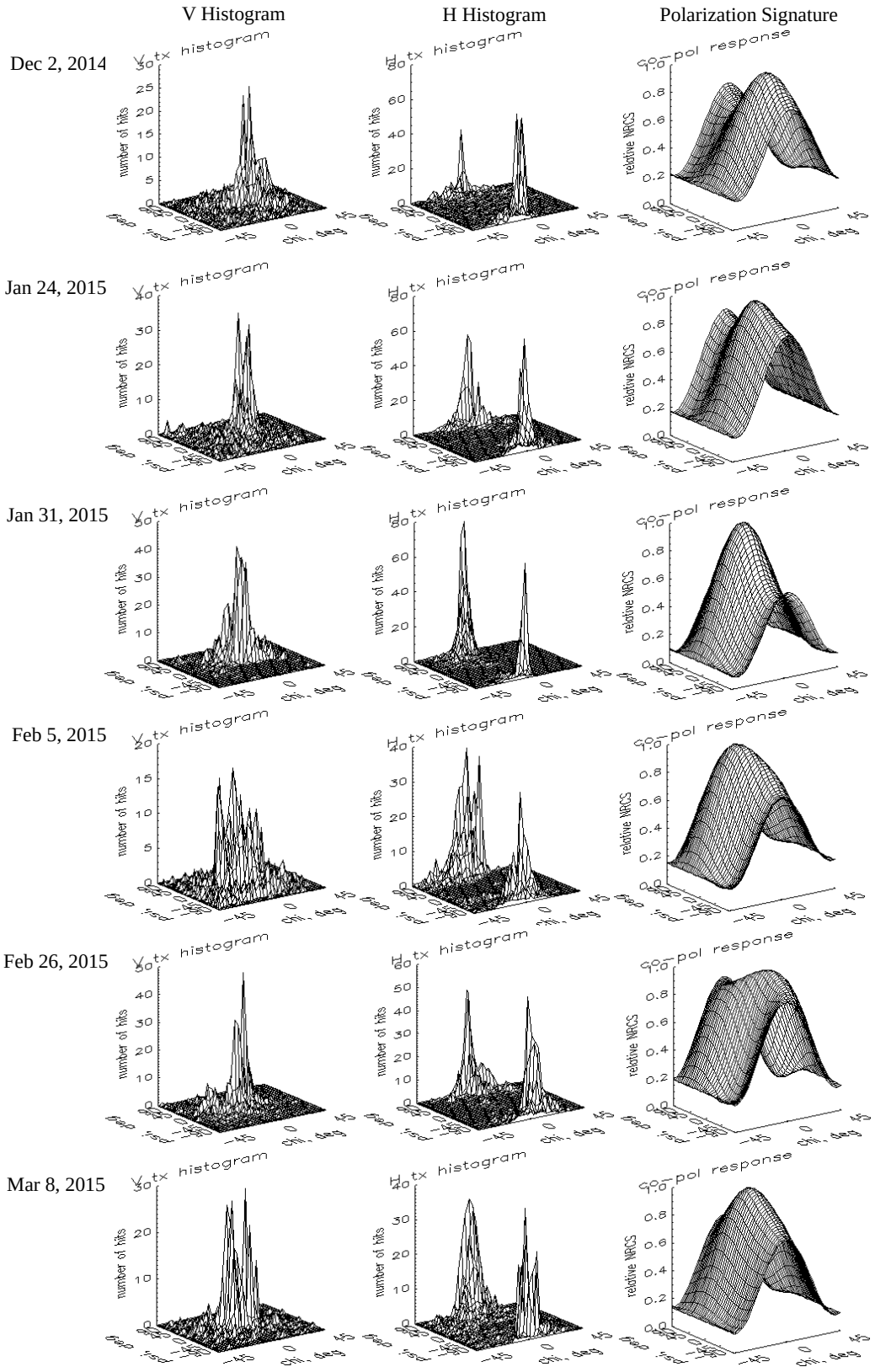

Figure A 4 Polarization histograms and signatures for X-band, 2014-15 season, Zinger site.

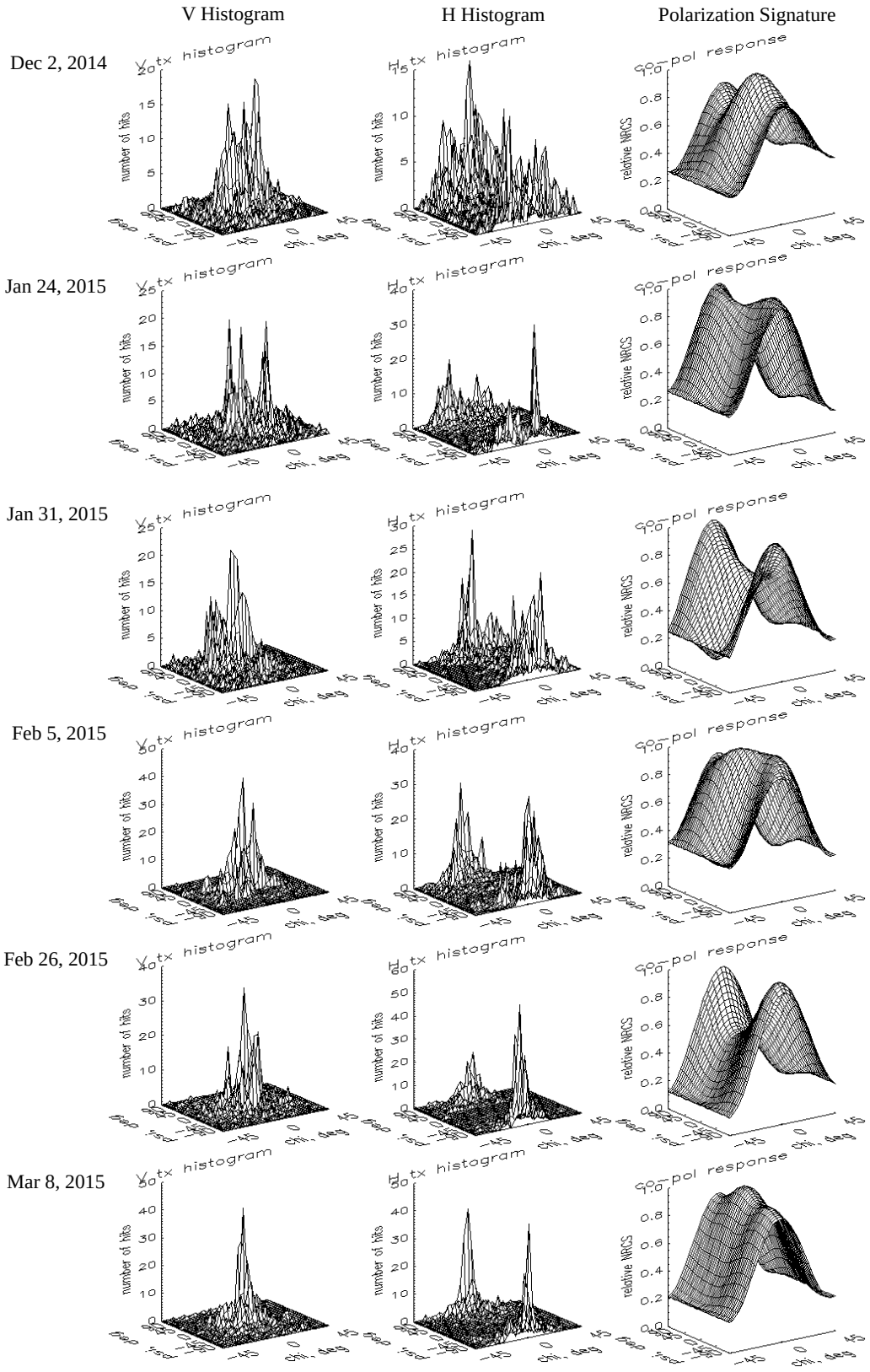

Figure A 5 Polarization histograms and signatures for Ku-band, 2014-15 season, John's farm.

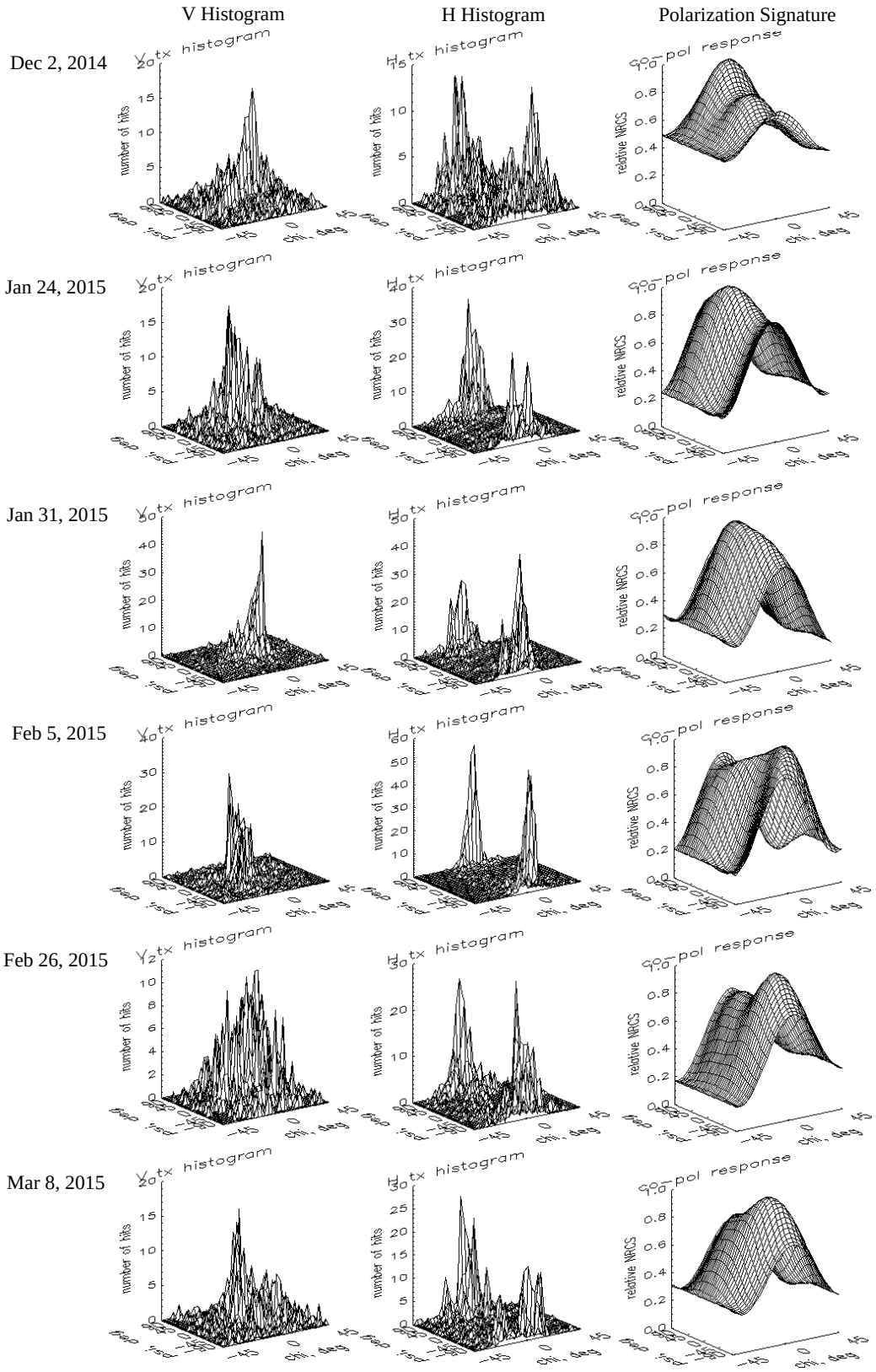

Figure A 6 Polarization histograms and signatures for X-band, 2014-15 season, John's farm.

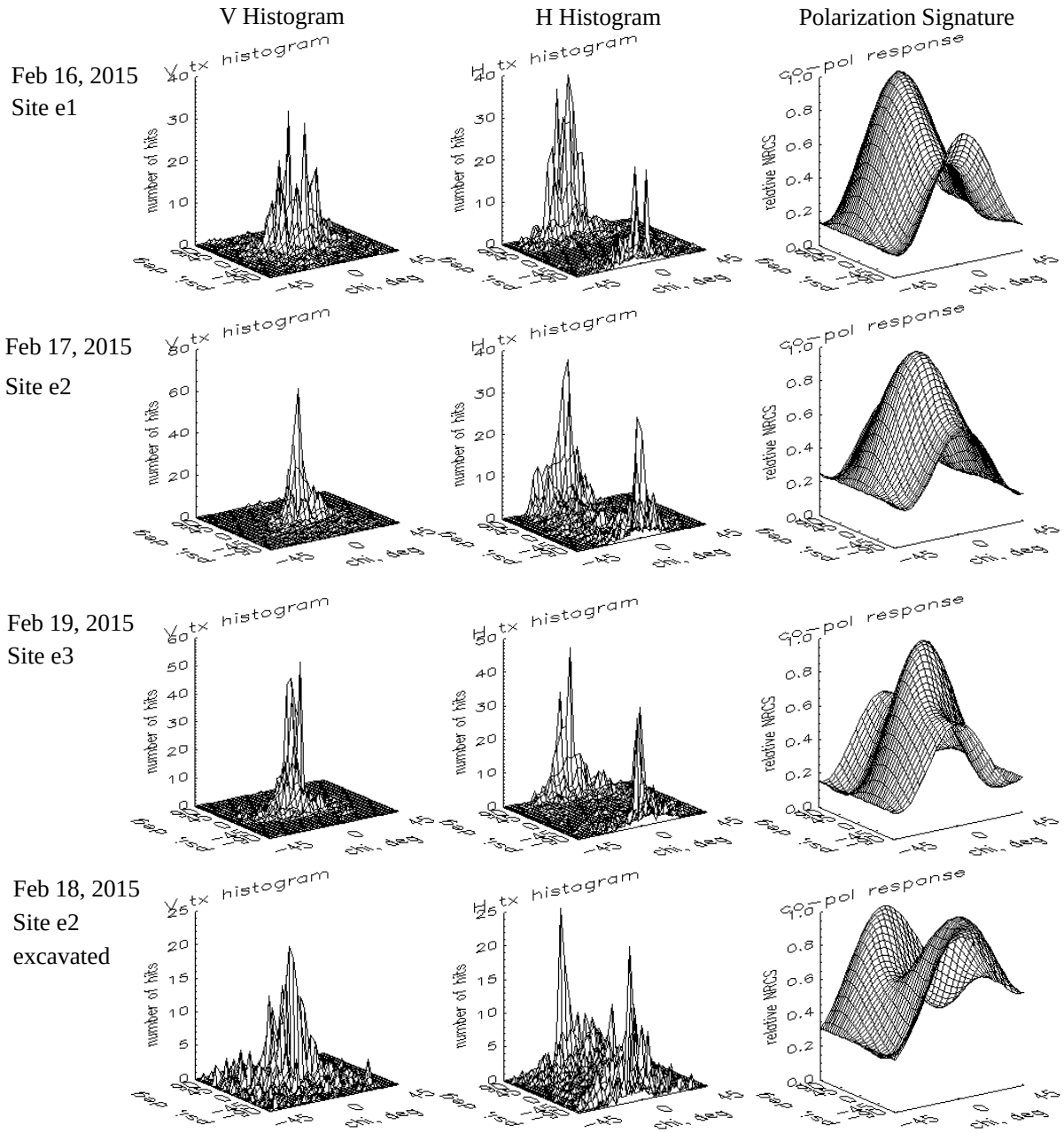

Figure A 7 Polarization histograms and signatures for Ku-band, 2014-15 season, Englehart.

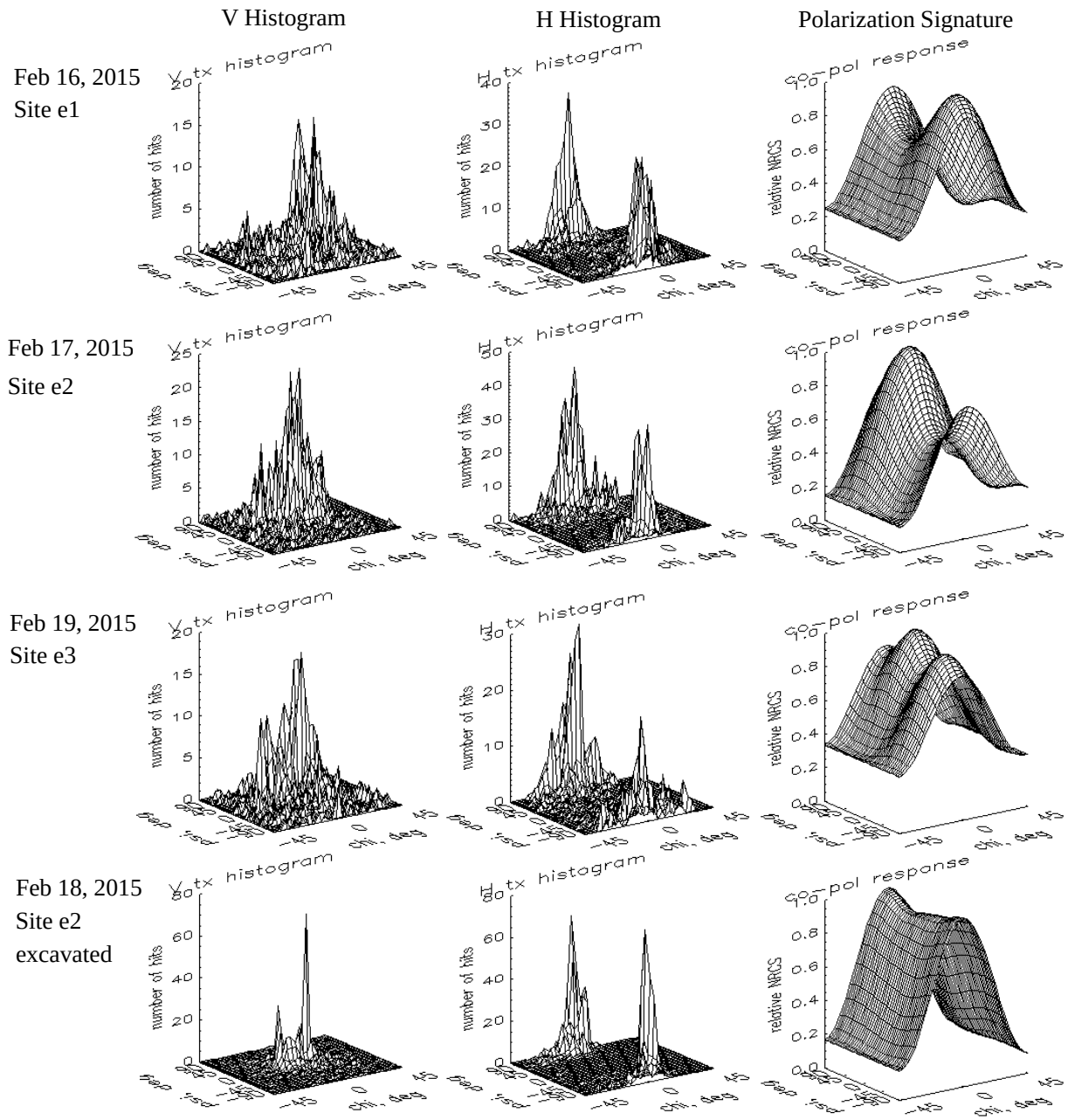

Figure A 8 Polarization histograms and signatures for X-band, 2014-15 season, Englehart.

B Sample calculation for density-weighted grain size (DWGS)

This sample calculation shows the procedure used to calculate DWGS. Data used in this calculation is for demonstration only and does not represent observed conditions.

Layer Number	Layer Density ($kg\ m^{-3}$)	Long Axis Grain Size (mm)	Calculation	Density Weighting (unitless)	Calculation	DWGS per Layer (mm)
1	200	0.5	200 / 1290 =	0.155	0.5 X 0.155 =	0.08
2	240	0.8	240 / 1290 =	0.186	0.8 X 0.186 =	0.15
3	300	1	300 / 1290 =	0.233	1 X 0.233 =	0.23
4	220	2	220 / 1290 =	0.171	2 X 0.171 =	0.34
5	330	3	330 / 1290 =	0.256	3 X 0.256 =	0.77
SUM=	1290		**SUM =**	1.000	**SUM=**	1.57
					TOTAL DWGS (mm)=	**1.57**

References

Attema, E. P. W., & Ulaby, F. T. (1978). Vegetation modeled as a water cloud. *Radio Science*, *13*(2), 357.

Barnett, T. P., Adam, J. C., & Lettenmaier, D. P. (2005). Potential impacts of a warming climate on water availability in snow-dominated regions. *Nature*, *438*(7066), 303–309.

Benson, C., & Sturm, M. (1993). Structure and wind transport of seasonal snow on the Arctic slope of Alaska. *Annals of Glaciology*, *18*, 261–267.

Bormann, K. J., Westra, S., Evans, J. P., & McCabe, M. F. (2013). Spatial and temporal variability in seasonal snow density. *Journal of Hydrology*, *484*, 63–73.

Brown, R. D., & Mote, P. W. (2009). The response of northern hemisphere snow cover to a changing climate. *Journal of Climate***,** 22(8), 2124–2145.

Colbeck, S.C. (1980). Thermodynamics of snow metamorphism due to variations in curvature. *J. Glaciol*., 26(94), 291–301.

Colbeck, S. C. (1982a). An overview of seasonal snow metamorphism. *Reviews of Geophysics*, 20(1), 45-61.

Colbeck, S. C. (1982b). The geometry and permittivity of snow at high frequencies. *Journal of Applied Physics*, *53*(6), 4495–4500.

Debeer, C. M., & Pomeroy, J. W. (2009). Modelling snow melt and snowcover depletion in a small alpine cirque, Canadian Rocky Mountains, *23*(18), 2584–2599.

Derksen, C., & Brown, R. (2012). Spring snow cover extent reductions in the 2008-2012 period exceeding climate model projections. *Geophysical Research Letters*, *39*(19), 1–6.

Dierking, W., Linow, S., & Rack, W. (2012). Toward a robust retrieval of snow accumulation over the Antarctic ice sheet using satellite radar. *Journal of Geophysical Research*, *117*(D9), D09110.

DMTI CanMap (computer file). Markham, Ontario: DMTI Spatial Inc., (2014).

Du, J., Shi, J., & Rott, H. (2010). Comparison between a multi-scattering and multi-layer snow scattering model and its parameterized snow backscattering model. *Remote Sensing of Environment*, *114*(5), 1089–1098.

Durand, M., Kim, E. J., & Margulis, S. A. (2008). Quantifying uncertainty in modeling snow microwave radiance for a mountain snowpack at the point-scale, including stratigraphic effects. *IEEE Transactions on Geoscience and Remote Sensing*, *46*(6), 1753–1767.

Elachi, C., Kuga, Y., McDonald, K.C., Sarabandi, K., Senior, T.B.A., Ulaby, F.T., van Zyl, J.J., Whitt, M.W., & Zebker, H.A. (1990). *Radar polarimetry for geoscience applications.* Ulaby, F.T., Elachi, C. (Ed.). Norwood: Artech House Inc.

Environment Canada. (2015). *Canadian Climate Normals*. Retrieved June 01, 2015, from http://climate.weather.gc.ca/climate_normals/index_e.html.

ESRI. (2014). Basemap. Redlands, CA: Environmental Systems Research Institute.

Evans, D. L., Farr, T.G., Van Zyl, J.J., & Zebker, H.A. (1988). Radar polarimetry: analysis tools and applications. *IEEE Transactions on Geoscience and Remote Sensing,* 26(6), 774-789.

Fierz, C., Armstrong, R.L., Durand, Y., Etchevers, P., Greene, E., McClung, D.M., Nishimura, K., Satyawali, P.K. and Sokratov, S.A. 2009. The International Classification for Seasonal Snow on the Ground. *IHP-VII Technical Documents in Hydrology N°83, IACS Contribution N°1, UNESCO-IHP*, Paris.

Forster, R. R., Davis, C. H., Rand, T. W., & Moore, R. K. (1991). Snow-stratification investigation on an Antarctic ice stream with an X-band radar system, *Journal of Glaciology, 37*(127), 323–325.

Helbig, N., & van Herwijnen, A. (2012). Modeling the spatial distribution of surface hoar in complex topography. *Cold Regions Science and Technology*, *82*, 68–74.

Hoffman, D.W., Wicklund, R.E., & Richards, N. R. (1972). Soil survey of New Liskeard-Englehart area. *The Ontario Soil Survey*, (21).

IGOS (2007). Integrated Global Observing Strategy Cryosphere Theme Report – For the Monitoring of our Environment from Space and from Earth. Technical Report WMO/TD-No1405, IGOS.

Kendra, J. R., Sarabandi, K., & Ulaby, F. T. (1998). Radar measurements of snow : experiment and analysis. *IEEE Transactions on Geoscience and Remote Sensing*, *36*(3), 864–879.

King, J. M. L., Kelly, R., Kasurak, A., Duguay, C., Gunn, G., & Mead, J. B. (2013). UW-Scat : a ground-based dual-frequency scatterometer for observation of snow properties. *IEEE Geoscience and Remote Sensing Letters*, 10(3), 528–532.

King, J., Kelly, R., Kasurak, A., Duguay, C., Gunn, G., Rutter, N., Derksen, C. (2015). Spatio-temporal influence of tundra snow properties on Ku-band (17.2 GHz) backscatter. *Journal of Glaciology*, *61*(226), 267–279.

Koh, G., Yankielun, N.E., & Baptista, A.I. (1996). Snow cover characterization using multiband FMCW radars. *Hydrological Processes,* (10), 1609-1617

Langlois, A., Mundy, C. J., & Barber, D. G. (2007). On the winter evolution of snow thermophysical properties over land-fast first-year sea ice. *Hydrological Processes*, 21(6), 705–716.

Lemmetyinen, J., Kontu, A., Leppänen, L., Pulliainen, J., Wiesmann, A., Werner, C., Proksch, M., & Schneebeli, M. (2013). Technical assistance for the development of an X- to Ku-band scatterometer during the NoSRExIII experiment, Final report, ESA ESTEC Contract No. 22671/09/NL/JA, European Space Agency ESA ESTEC.

López-Moreno, J. I., Fassnacht, S. R., Heath, J. T., Musselman, K. N., Revuelto, J., Latron, J., Morán-Tejeda, & Jonas, T. (2013). Small scale spatial variability of snow density and depth over complex alpine terrain: Implications for estimating snow water equivalent. *Advances in Water Resources*, *55*, 40–52.

MacDonald, M. K., Pomeroy, J. W., & Pietroniro, A. (2010). On the importance of sublimation to an alpine snow mass balance in the Canadian Rocky Mountains. *Hydrology and Earth System Sciences*, *14*(7), 1401–1415.

Marsh, P. (2005). Water flow through snow and firn. In M. G. Anderson (Ed.), *Encyclopedia of Hydrological Sciences*, (pp 1-14). Wiley: Canada.

Marsh, P. (1987). Grain growth in a wet arctic snow cover. *Cold Regions Science and Technology*, *14*(1), 23–31.

Marsh, P., & Woo, M.-K. (1984). Wetting front advance and freezing of meltwater within a snow cover 1. Observations in the Canadian arctic. *Water Resources Research*, *20*(12), 1853–1864.

Marshall, S.J. (2012). *The Cryosphere*. Princeton: Princeton University Press.

Marshall, H.-P., & Koh, G. (2008). FMCW radars for snow research. *Cold Regions Science and Technology*, *52*(2), 118–131.

Marshall, H. P., Koh, G., & Forster, R. R. (2005). Estimating alpine snowpack properties using FMCW radar. *Annals of Glaciology*, *40*(1998), 157–162.

Marshall, H.-P., Koh, G., & Forster, R. R. (2004). Ground-based frequency-modulated continuous wave radar measurements in wet and dry snowpacks, Colorado, USA: an analysis and summary of the 2002-03 NASA CLPX data. *Hydrological Processes*, *18*(18), 3609–3622.

Marshall, H.-P., Schneebeli, M., & Koh, G. (2007). Snow stratigraphy measurements with high-frequency FMCW radar: Comparison with snow micro-penetrometer. *Cold Regions Science and Technology*, *47*(1-2), 108–117.

Mätzler, C. (1987). Applications of the interaction of microwaves with the natural snow cover. *Remote Sensing Reviews*, *2*(2), 259–387.

McNairn, H., Duguay, C., Boisvert, J., Huffman, E., & Brisco, B. (2001). Defining the sensitivity of multi-frequency and multi-polarized radar backscatter to post-harvest crop residue. *Canadian Journal of Remote Sensing*, *27*(3), 247–263.

McNairn, H., Duguay, C., Brisco, B., & Pultz, T. J. (2002). The effect of soil and crop residue characteristics on polarimetric radar response. *Remote Sensing of Environment*, *80*, 308–320.

Painter, T. H., Molotch, N. P., Cassidy, M. P., Flanner, M., & Steffen, K. (2007). Contact spectroscopy for the determination of stratigraphy of snow grain size. *Journal of Glaciology*, *53*(180), 121–127.

Pomeroy, J. W., Gray, D. M., Shook, K. R., Toth, B., Essery, R. L. H., Pietroniro, A., & Hedstrom, N. (1998). An evaluation of snow accumulation and ablation processes for land surface modelling. *Hydrological Processes*, *12*(15), 2339–2367.

Pomeroy, J., MacDonald, M., DeBeer, C., & Brown, T. (2009). Modelling alpine snow hydrology in the Canadian Rocky Mountains. *Western Snow Conference 2009*.

Presant, E.W., Wicklund, R.E. (1971). The soils of Waterloo county. *The Ontario Soil Survey*, (44).

Proksch, M., Löwe, H., & Schneebeli, M. (2015a). Density, specific surface area and correlation length of snow measured by high-resolution penetrometry. *J. Geophys. Res.-Earth Surface*, 346-362.

Proksch, M., Mätzler, C., Wiesmann, A., Lemmetyinen, J., Schwank, M., Löwe, H., & Schneebeli, M. (2015b). MEMLS3&a: Microwave Emission Model of Layered Snowpacks adapted to include backscattering. *Geoscientific Model Development Discussions*, *8*(3), 2605–2652.

Regional Municipality of Waterloo Streets and Planning Data (computer file). Kitchener, Ontario: Regional Municipality of Waterloo, (2014).

Rott, H., Yueh, S. H., Cline, D. W., Duguay, C., Essery, R., Haas, C., Hélière, F., Kern, M., Macelloni, G., Malnes, E., Nagler, T., Pulliainen, J., Rebhan, H., & Thompson, A. (2010). Cold Regions Hydrology High-Resolution Observatory for snow and cold land processes. *Proceedings of the IEEE*, 98(5), 752–765.

Schweizer, J., & Kronholm, K. (2007). Snow cover spatial variability at multiple scales: Characteristics of a layer of buried surface hoar. *Cold Regions Science and Technology*, *47*(3), 207–223.

Shi, J. S. J. (2004). Estimation of snow water equivalence with two Ku-band dual polarization radar. *IGARSS 2004. 2004 IEEE International Geoscience and Remote Sensing Symposium*, *3*(C), 1649–1652.

Shi, J., & Dozier, J. (2000). Estimation of snow water equivalence using SIR-C/X-SAR, part I: Inferring snow depth and particle size. *IEEE Transactions on Geoscience and Remote Sensing*, 38(6), 2475–2488.

Strozzi, T., & Mätzler, C. (1998). Backscattering measurements of alpine snowcovers at 5.3 and 35 GHz. *IEEE Transactions on Geoscience and Remote Sensing*, 36(3), 838–848.

Sturm, M., & Benson, C. (1997). Vapor transport, grain growth and depth-hoar development in the subarctic snow. *Journal of Glaciology*, 43(143), 42-59.

Sturm, M., & Benson, C. (2004). Scales of spatial heterogeneity for perennial and seasonal snow layers, *Annals of Glaciology*, 38, 253–260.

Sturm, M., Holgmren, J., & Liston, G. E. (1995). A seasonal snow cover classification system for local to global applications. *Journal of Climate*, 8(5), 1261-1283.

Sturm, M., Johnson, J., Holmgren, J., 2004. Variations in the mechanical properties of arctic and subarctic snow at local (1-m) to regional (100-km) scales. *In Proceedings of the International Symposium on Snow Monitoring and Avalanches* (ISSMA-2004), Manali, India.

Sturm, M., Taras, B., Liston, G. E., Derksen, C., Jonas, T., & Lea, J. (2010). Estimating snow water equivalent using snow depth data and climate classes. *Journal of Hydrometeorology*, *11*(6), 1380–1394.

Tape, K. D., Rutter, N., Marshall, H. P., Essery, R., & Sturm, M. (2010). Instruments and methods recording microscale variations in snowpack layering using near-infrared photography. *Journal of Glaciology*, *56*(195), 75–80.

Tiuri, M.E., Sihvola, A.H., Nyfors, E.G., & Hallikainen, M.T. (1984). The complex dielectric constant of snow at microwave frequencies. *IEEE Journal of Oceanic Engineering*, 9(5), 377-382.

Ulaby, F., & Batlivala, P. (1976). Diurnal variations of radar backscatter from a vegetation canopy. *IEEE Transactions on Antennas and Propagation*, *24*(1), 11–17.

Ulaby, F., Bush, T.F., & Batlivala, P.P. (1975). Radar response to vegetation II: 8-18 GHz band. *Antennas and Propagation, IEEE Transactions on*, (5), 608–618.

Ulaby, F.T., Moore, R.K., & Fung, A.K. (1981). Microwave Remote Sensing – Active and Passive – Volume 1 – Radar Remote Sensing and Surface Scattering and Emission Theory. Norwood: Artech House Inc.

Ulaby, F.T., Moore, R.K., & Fung, A.K. (1982). Microwave Remote Sensing – Active and Passive – Volume 2 – Radar Remote Sensing and Surface Scattering and Emission Theory. Norwood: Artech House Inc.

Ulaby, F.T., Moore, R.K., & Fung, A.K. (1986). Microwave Remote Sensing – Active and Passive – Volume 3 – From Theory to Applications. Norwood: Artech House Inc.

Ulaby, F.T., & Long, D.G. (2014). *Microwave radar and radiometric remote sensing*. Ann Arbor: The University of Michigan Press.

Ulaby, F. T., & Stiles, W. H. (1981). Microwave response of snow. *Advances in Space Research*, (1), 131-149.

Ulaby, F., Stiles, W., & Abdelrazik, M. (1984). Snowcover influence on backscattering from terrain. *IEEE Transactions on Geoscience and Remote Sensing*, (2), 126–133.

Wakahama, G. (1965). Metamorphism of wet snow. *Low temp. Sci.* A(23), 51-66.

Wegmüller, U. (1990). The effect of freezing and thawing on the microwave signatures of bare Soil. *Remote Sensing of the Environment*, (135), 123–135.

Wiesmann, A., & Ma, C. (1999). Microwave Emission Model of Layered Snowpacks. *Remote Sensing of the* Environment, (70), 307-316.

Woodhouse, I. (2006). Introduction to microwave remote sensing. Boca Raton: CRC Press.

WMO (1997). Global Climate Observing System: GCOS/GTOS Plan for terrestrial climate-related observations, Version 2.0. Technical Report WMO/TD-No 796, WMO.

Yueh, S. H., Dinardo, S. J., Akgiray, A., West, R., Cline, D. W., & Elder, K. (2009). Airborne Ku-Band polarimetric radar remote sensing of terrestrial snow cover. *IEEE Transactions on Geoscience and Remote Sensing*, 47(10), 3347–3364.